Local magnetizations in impure two-dimensional antiferromagnets

J. A. van Luijk, A. F. M. Arts, and H. W. de Wijn
Fysisch Laboratorium, Rijksuniversiteit, Post Office Box 80.000, 3508 TA Utrecht, The Netherlands
(Received 3 August 1979)

The local magnetizations near dilute substitutional impurities in the quadratic-layer antiferromagnet K_2MnF_4 are studied both experimentally and theoretically. The impurities considered are the nonmagnetic Zn and Mg, as well as Ni. The magnetizations are probed through the positions of the impurity-associated satellites in the nuclear magnetic resonance of the out-of-layer and in-layer ^{19}F nuclei adjacent to the magnetic ions. It is discussed in which way the effects of lattice deformations can be eliminated in order to obtain the variations of the local magnetizations with temperature. The theoretical treatment is based on Green's-function techniques. The decoupling employed is within the local spin-deviation operators and accounts for correlation between nearest neighbors. It reduces the renormalized spin-wave Hamiltonian to an effective quadratic form, rendering decoupling of Green's functions unnecessary. The spectral distributions of the excitations are calculated including local modes. The theory is subsequently applied to the 13-site cluster consisting of the impurity and the first three shells of Mn around it. Good agreement is found. The magnetization is significantly modified in the first shell. The further shells are only weakly affected, however somewhat stronger than in comparable three-dimensional systems. For nonmagnetic impurities the thermal spin deviation in the first shell is about $\frac{1}{3}$ larger than that of the host; in the Ni-doped system the additional deviations are within 1%. The zero-point deviation of the Ni is 0.11 units of spin, as compared to 0.17 in the host. A further experimental result is a uniform shift, increasing with concentration, of the sublattice magnetization at large distance from the impurity. It must be related to the finite density of states near the zone center in two-dimensional systems. Finally, some data are presented on the local susceptibilities.

I. INTRODUCTION

The local effect on the magnetization associated with the replacement of a limited number of spins in ordered magnetic systems by nonmagnetic ions or ones with other magnetic properties has been a long-standing problem in magnetism. Nonetheless, for Heisenberg antiferromagnets, studies dealing with the problem in detail amount to only a few. The reason for this probably is that the local magnetization at or near the impurity is not easily accessible to direct determination. The most detailed experimental information has, in fact, been provided by nuclear magnetic resonance (NMR), with which, under favorable circumstances, resonances associated with the first few shells about the impurity may be discerned from the host.

Theoretical treatments were first developed for impurities in ferromagnets,[1] and subsequently for antiferromagnets.[2,3] As the interaction between the impurities is expected to be small, even at experimentally useful concentrations, the theoretical description may conveniently be reduced to considering a *single* impurity, located in the origin of an otherwise perfect lattice. The problem is usually idealized by assuming that the exchange interactions beyond the first neighbors of the impurity are not affected. The perturbation of the pure system, which can be of substantial size at the impurity site itself, generally falls off within a few shells. The impurity problem may in principle be treated to all orders by use of Green's-function techniques. However, some kind of decoupling must be introduced to make the analysis tractable, and, as we will clearly see in this paper, the choice of the decoupling is extremely consequential in obtaining agreement with experimental findings. An important aspect further is the spectral density of the excitations, which is drastically altered near the impurity by modes of various sharpness. Under certain conditions part of the spectral density is transferred to very sharp localized modes outside the spin-wave band of the host. Such modes have indeed been identified above the band by Raman scattering.

The introduction of a nonmagnetic impurity amounts to cutting the exchange interactions between the impurity and the ions in the first shell. Accordingly, for a well-known host, there are no parameters with which to adjust theory to experiment. The Green's-function calculations of Walker *et al.*[2] have nevertheless been quite successful when compared with NMR results by Butler *et al.*[4] on Zn impurities

in the rutile-structure MnF_2 (MnF_2 is a Heisenberg antiferromagnet, but has the drawback that three Mn^{2+} ions contribute to the hyperfine fields at ^{19}F, making separate determination of Mn magnetizations difficult). A successful fit was also achieved for Fe-doped MnF_2, but not for Ni. The general conclusion of these studies is that the effect of an impurity on the magnetizations of its neighbors is essentially significant on the first shell only, and even there the modifications are minute ($\sim 1\%$). We will see that in two-dimensional (2-D) systems this conclusion will stand up to a great extent. More concentrated systems have also been studied. Since the results have some bearing on the impurity problem, we mention theoretical treatments in the regime of high concentration of impurities by the technique of configurational-averaged Green's-functions.[5]

In the present paper, we will deal with the local magnetization in the vicinity of an impurity in a 2-D system. The host chosen is the quadratic-layer structure K_2MnF_4, which is known to be a nearly genuine 2-D Heisenberg antiferromagnet.[6,7] The crystal structure is such that powerful NMR probes are available in the form of the ^{19}F nuclei adjacent to the Mn. These nuclei resonate in strong transferred hyperfine fields and permit direct measurement of the *individual* magnetizations at the various shells. Another important feature of the quadratic-layer structure is its simplicity. A single exchange parameter and a weak anisotropy, the latter of which is not very important to the problem, define the system from the magnetic point of view; the Brillouin zone is also quadratic. Obviously, this simplicity is advantageous in arriving at numerical results. The impurities considered are the nonmagnetic Zn and Mg, as well as Ni ($S=1$). The former have modes within the spin-wave continuum, the latter above because the Ni-Mn interaction is stronger than the exchange of the host. As already mentioned, the decoupling procedure used to solve the equations of motion of the Green's functions has important consequences on the energy renormalization and the spectral density, and thereby on the calculated magnetizations at the various shells. One specific objective of this study is to see the effects of the corrrelations between nearest neighbors, which were ignored in the treatment of Walker *et al.*

The paper is organized as follows. In Sec. II, we give details about the experimental techniques used, discuss the effects of small lattice deformations on the positions of the lines, and indicate how these effects can be eliminated. In Sec. III, a Green's-function treatment is developed. The decoupling procedure is employed locally. It includes the correlation between nearest neighbors, and reduces the impurity problem to a manageable form, even when including shells of neighbors beyond the first. The 2-D character, as reflected in the numerically evaluated Green's functions of the pure system, as well as the impurity-associated Green's functions are discussed in Sec. IV. In Sec. V, we outline the identification of the various NMR lines, and extract the experimental temperature dependence of the local magnetizations relative to the host. Subsequently, the magnetizations of the first three shells about the impurity as calculated with Green's functions are compared with experiment. Section V also contains some data on the local susceptibility. It further discusses a concentration-dependent shift of the magnetization far away from the impurity, which has not been observed in 3-D systems, and apparently is characteristic for two dimensions.

II. EXPERIMENTAL

The magnetizations of the various Mn^{2+} about the impurity were measured by tracking the NMR of the adjacent ^{19}F nuclei (Fig. 1). These nuclei resonate in strong transferred hyperfine fields originating from the magnetic ions, with additional dipolar contributions. In K_2MnF_4 with the magnetic field directed along the tetragonal axis, there are three distinct classes of fluor positions, with corresponding frequencies. The NMR frequencies of the out-of-layer $^{19}F^{I}$ nuclei, $f^{I}_{\uparrow}$ and $f^{I}_{\downarrow}$, reflect the individual magnetizations residing on the "up" and "down" Mn^{2+} ions, respectively. At zero temperature and zero external field, $f^{I}_{\uparrow}=f^{I}_{\downarrow}\approx 150$ MHz.[7] The $^{19}F^{II}$ nuclei, located in the layer, resonate with frequency f^{II} in the net transferred hyperfine field of two antiferromagnetically coupled Mn neighbors and a smaller dipolar field resulting from a summation over the lattice. The f^{II} frequency thus reflects the unbalance between the two neighbors. In zero field, f^{II} of course vanishes in pure K_2MnF_4.

Experimentally, the NMR was performed at fixed frequency in a variable external field ranging from 0 to 14 kG. This is far more simple than varying the frequency in a zero-field experiment, where one must ensure that transmitter, receiver, and tuned resonance circuit track accurately. When parallel to the c axis, the external field is simply additive, apart from negligible corrections, to the hyperfine field with the sign dependent on the particular ^{19}F. At 105.300 ± 0.001 MHz, the frequency mostly used for the out-of-layer ^{19}F, the $^{19}F^{I}_{\downarrow}$ resonances at 4.2 K are detected at external fields of about 11 kG. As a typical example, the $^{19}F^{I}_{\downarrow}$ NMR spectrum in a Zn-doped crystal at 4.2 K is given in Fig. 2. In addition to the main resonance associated with Mn^{2+} ions at large distances from the impurity as well as dipolar-shifted resonances of $^{19}F^{I}$ in neighboring layers, the spectrum contains a number of weaker lines originating from $^{19}F^{I}_{\downarrow}$ nuclei close to the impurity. The positions of the latter contain the information on the magneti-

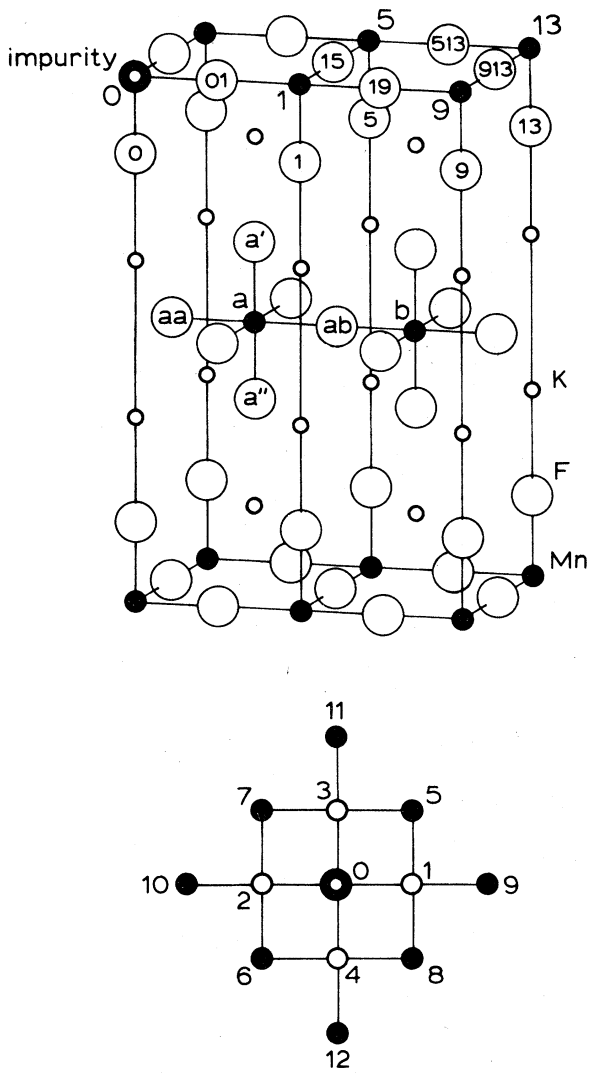

FIG. 1. Part of the K_2MnF_4 lattice containing a substitutional impurity, with labeling of the Mn and ^{19}F sites. Lower part of the figure shows the cluster of 13 lattice sites on which the Green's-function calculations were done. The impurity, the second and third shell are on the up sublattice, the first shell is on the down sublattice.

zations near the impurity. When detecting the in-layer $^{19}F^{II}$, the spectrometer was set at 40.000 ± 0.001 MHz, yielding resonance in external fields of about 10 kG over the whole temperature range up to 45 K. Here the magnetizations at neighboring Mn^{2+} largely cancel, even in the vicinity of the impurity. Therefore, the resonance fields are close to that of a free ^{19}F. The information on the magnetizations about the impurity is again contained in a number of weaker satellite resonances, but with the notable difference that the spectra are symmetric about the main resonance, at least at low temperatures.

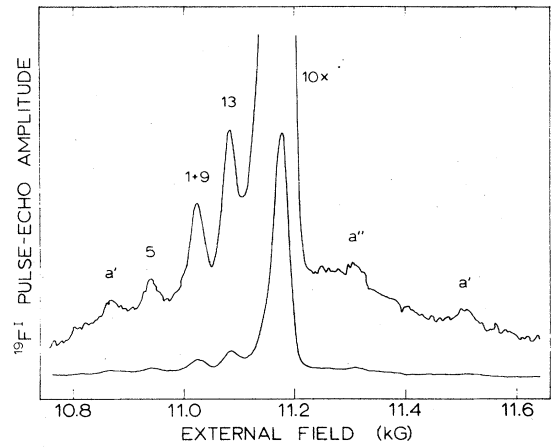

FIG. 2. Pulse-echo $^{19}F^{I}$ NMR spectrum ($f = 105.300$ MHz) of 0.4-at.% Zn-doped K_2MnF_4 at 4.2 K. The main resonance originates from $^{19}F^{I}_{\downarrow}$ far away from the impurity. At 4.2 K, the resonances from $^{19}F^{I}_{(1)}$ and $^{19}F^{I}_{(9)}$ nearly coincide.

Precise values for the hyperfine interactions in pure ordered K_2MnF_4 have earlier been obtained from a spin-wave analysis of NMR data.[8] The result for the in-layer hyperfine interaction constant is $|A^{II}| = 51 \pm 1$ MHz per unit of spin. Reworking the analysis of Ref. 8 with 2.105 Å for the distance Mn-F^{I}, we find for the out-of-layer hyperfine interaction constant $|A^{I}| = 48.3 \pm 1.0$ MHz per unit of spin.[9] At this point it should, however, be emphasized that these constants are extremely sensitive to variations of interatomic distances. Replacing a Mn ion by an impurity with a different ionic radius may cause a local change in the Mn-F separations of a few hundredths of an angstrom, resulting in a change of a few percent in the hyperfine interaction constants. We will consider these effects in more detail in Sec. II B.

A. Experimental details

Single crystals of K_2MnF_4 were grown from the melt with a horizontal zone-melting technique and had a typical size of 40 mm^3. For pure crystals of K_2MnF_4, the starting materials are zone-refined KF and $KMnF_3$. To obtain good single crystals without strain, elimination of temperature fluctuations in the zone appeared to be essential. At 4.2 K the dimensions of the tetragonal unit cell are $a = 4.151$ Å and $c = 13.242$ Å.[10] In growing doped crystals, we replaced up to 2.5 at.% of the $KMnF_3$ by KXF_3, with X = Zn, Mg, or Ni, depending on the dope desired. The dope concentration of the crystals was measured by the method of atomic absorption at various positions along the platinum boat; concentrations of other impurities were typically less than 50 ppm. The crystals cleave parallel to the a-b plane, which permits

determination of the c axis within a few tenths of a degree. This was verified by observing Laue diffraction patterns.

Temperature stabilization below 4.2 K was performed by servo-controlled pumping of the liquid He in which the sample was immersed, above 4.2 K by controlled heating of a continuous He gas flow. A second servo-controlled heater close to the sample holder further reduced fluctuations of the temperature. The residual short-term temperature stability was better than 0.01 K, the long-term stability better than 0.05 K. Temperatures were measured with a carbon-glass resistor, which is insensitive to magnetic fields, and a germanium resistor, both carefully calibrated against standard platinum and germanium resistors with an estimated inaccuracy of 20 mK below 4.2 K, increasing to 50 mK at 20 K. To check the reproducibility of the carbon-glass resistor, it was recalibrated with respect to the germanium resistor *in situ* at regular intervals of time, but any drift appeared to be minor. In the following analysis (Sec. II B) the inaccuracy in temperature, which was the major source of the experimental uncertainties, has been propagated additively to the error in the resonance fields. As already said, fields up to 14 kG parallel to the c axis have been used. The alignment was better than 1° of arc, and the field homogeneity was 0.1 G over a sphere of 2 cm diameter. With a sweep range of 1 kG, the sweep-tracking accuracy amounts to a few Gauss.

The NMR was mostly observed with two-pulse spin-echo techniques. Additionally, a number of data were taken in the continuous mode, permitting higher frequencies and correspondingly lower fields in our experimental arrangement. With spin echo, short coherent pulses from a crystal-stabilized standard oscillator were fed into an amplifier gated synchronously with the pulses and followed by a high-power amplifier stage. The detection of the NMR signal was done with a tunable VHF receiver with fast recovery after overload. The transmitter as well as the receiver were coupled to the coil wound around the sample. The receiver was isolated from the transmitter and protected against severe overload by suitable matching circuits, consisting of diodes and $\frac{1}{4}\lambda$ lines. The coil, in series with a variable capacitor, was tuned to the oscillator frequency. By letting the spin-echo signal following the second pulse interfere with the standard oscillator in a double-balanced mixer, a dc envelope of the spin-echo signal was obtained, given the fixed phase between standard oscillator and spin echo. After integration and sampling of the dc envelope, the spin-echo signal was stored in a multichannel analyzer with the x axis coupled to the magnetic field. Repetitive scanning in combination with averaging techniques was necessary to distinguish the weak impurity-related resonances from the noise. The typical signal-to-noise ratio of the main resonance after a single pass through the line was 60:1 at 4.2 K. The ratio however rapidly decreases with temperature partly due to the rapid decrease of the relaxation times T_1 and T_2. In pure K_2MnF_4 the longitudinal relaxation time T_1 at 4.2 K is of the order of 2 s.[11] No systematic study of the relaxation time T_1 has been carried out. From the saturation characteristics it seems however that the relaxation times in the doped crystals are not drastically different, excepting the $^{19}F^{I}$ adjacent to a nonmagnetic impurity, which relaxes more slowly by at least two orders of magnitude. The $^{19}F^{II}$ associated with the impurity and its nearest Mn neighbors appears to have slightly shorter relaxation times.

In pure K_2MnF_4, inhomogeneous line broadening is negligible. As a result the free-induction decay following a $\frac{1}{2}\pi$ pulse is slow, of the order of T_2 ($\sim 50\mu$s at 4.2 K), which prohibits the use of two-pulse spin-echo. In the impure systems, on the contrary, inhomogeneous broadening causes the free-induction to decay within a few μs. Therefore, the second pulse after a delay time of say 10μs refocusses the spins to a sharp spin echo. Because T_2 processes rapidly become more effective with increasing temperature, it is imperative for observing NMR at higher temperatures that the pulse sequence is compressed in time. At 4.2 K, typical durations used for the first pulse, the delay, and the second pulse were 3, 7, and 3μs, respectively. For pure K_2MnF_4 we measured a linewidth of 10 G at 4.2 K, which provides an upper limit for the instrumental width. At liquid-He temperatures, we found an NMR linewidth of 13 G for 0.5-at.% Ni dope in K_2MnF_4 (from cw measurements), 65 G for 2-at.% Ni, and 80 G for 3-at.% Ni. For Zn-doped K_2MnF_4 the linewidth at liquid He is 32 G for a concentration of 0.4-at.%, and 65 G for 0.8-at.%, while for the other nonmagnetic impurity, Mg, we measured 130 G for 2.2-at.%. It is noted that the width as well as its proportionality with concentration are in agreement with the calculated dipolar broadening by the electronic spins based on Van Vleck's method of moments. As examples, the calculation gives 65 G for 2-at.% Ni in K_2MnF_4, and 123 G for 2.2-at.% Mg.

B. Analysis of resonance fields

As we have seen, an impurity produces a number of satellite resonances in the ^{19}F NMR spectra of K_2MnF_4. The distances of these resonances relative to the main resonance are in fact a minute fraction of the hyperfine interaction itself (~ 1 MHz out of 150 MHz). The variations of the magnetizations at the various shells of Mn sites about the impurity (Fig. 1) are similarly small. In a detailed analysis of the displacements of the resonance fields leading to deter-

mination of the magnetizations, we may therefore not ignore that the impurity introduces local deformations of the lattice, which may complicate matters by altering the transferred and dipolar hyperfine interaction constants. Additionally, transferred hyperfine interactions of ^{19}F with second-neighbor magnetic ions (e.g., of $^{19}F^{I}_{(1)}$ with the impurity, or $^{19}F^{II}_{(01)}$ with $Mn_{(5)}$; for labeling of the sites see Fig. 1), known to be of the order of 1% of the primary hyperfine interaction, may be substantially modified when the impurity site is involved, and therefore produce effects of magnitude not very much smaller than the magnetic variations.

As a case in point, let us consider the out-of-layer $^{19}F^{I}_{(1)}$ adjacent to the Mn nearest to the impurity. For a single impurity with spin $\langle S^z_0 \rangle$, placed in an infinite lattice at position 0, its NMR frequency $f^{I}_{(1)}$ changes by the amount

$$\delta f^{I}_1 = (A^I + D^{I}_{11} + \delta A^I + \delta D^{I}_{11})(\langle S^z_\infty \rangle + \langle \delta S^z_1 \rangle) - (A^I + D^{I}_{11})\langle S^z_\infty \rangle + (B^I + D^{I}_{10} + \delta B^I + \delta D^{I}_{10})\langle S^z_0 \rangle - (B^I + D^{I}_{10})\langle S^z_\infty \rangle \ , \quad (1)$$

where the variations due to the substitution are denoted by the prefix δ; $\langle S^z_\infty \rangle$ is the sublattice magnetization at sites far away from an impurity (for extreme dilution equal to that of the pure lattice), and accordingly $\langle \delta S^z_1 \rangle$ its variation at position 1; A^I is the transferred hyperfine constant; D^{I}_{10} and D^{I}_{11} are the dipolar hyperfine constants for $^{19}F^{I}_{(1)}$ due to the moments at positions 0 and 1, respectively (values of dipolar interaction for various lattice sites are given in Table I); and B^I is the second-neighbor hyperfine interaction constant for the $^{19}F^{I}$ sites. In Eq. (1), smaller effects, such as due to variation of the magnetization at site 5, are ignored. Similar expressions may of course be written down for the other $^{19}F^{I}$ positions and the various $^{19}F^{II}$, the latter however with contributions from two oppositely aligned first Mn neighbors.

The effects of lattice deformations make the situation quite difficult to handle, the more so because detailed knowledge on the deformations is not available. In fact, some information on local deformations may be gathered from our data. Further, the results of EPR and NMR under high pressure in the undiluted magnetic systems as well as in systems with magnetic impurities in nonmagnetic hosts have some bearing on our problem. We will review these first in some detail for a judgment on the magnitude of the effects, and then return to Eq. (1).

TABLE I. Dipolar fields at various positions, labeled according to Fig. 1, due to a unit spin ($g = 2$) at the impurity site.

Position of $^{19}F^{I}$	Dipolar field (kG/unit of spin)	Position of $^{19}F^{II}$	Dipolar field (kG/unit of spin)
0	+3.98	01	−2.07
1	−0.07	15	−0.19
5	−0.05	19	−0.08
9	−0.02	513	−0.04
13	−0.02	913	−0.03
a'	+0.13	aa	+0.10
a''	+0.04	bb	+0.04

We first discuss the hyperfine constants A^I and A^{II}. An impurity generally has an electronic configuration and ionic radius different from the magnetic ion of the host. The lattice constants of K_2XF_4 with X = Mn, Zn, Mg, and Ni are tabulated in Table II, along with the X-F^I and X-F^{II} separations and effective ionic radii of the ions X^{2+}. In comparing the a and c axes with the ionic radii, we see that there is no simple relation between the lattice constants and the radii. The hyperfine interaction is however strongly dependent on the X-F distance. Pressure-dependent NMR yields a dependence of $(2.5 \pm 0.5) \times 10^2$ MHz Å^{-1} in MnF_2,[12] i.e., a 0.02 Å dilation of Mn-F already results in a 10% change of the hyperfine interaction. From the difference between A^I and A^{II} in pure K_2MnF_4 even a variation according to $(3.3 \pm 0.9) \times 10^2$ MHz Å^{-1} was derived.[13] Further, data are available on the transferred hyperfine interaction in related Mn-doped diamagnetic systems (K_2XF_4:Mn with X = Zn, Mg, and KXF_3:Mn with X = Mg, Cd) and in $KMnF_3$.[14–17] Comparing the isotropic part of the transferred hyperfine interaction in the diluted systems with those in the pure Mn ones (Fig. 3), we note that in the former the distance Mn-F is apparently shifted from the distance X-F of the host towards Mn-F in the corresponding Mn compounds, i.e., deformations in the first shell of a few 0.01 Å. In further shells, the variations will be substantially smaller by roughly a factor of 4 per shell.[18] Similar deformations are expected to occur about the impurity in doped K_2MnF_4, with corresponding variations in the hyperfine structure.

In addition to the direct hyperfine interaction with the adjacent Mn^{2+}, the hyperfine field at the F nuclei has contributions from second-neighbor Mn ions. Orbital overlap between neighboring fluorines and

TABLE II. Lattice parameters of the compounds K_2XF_4 at the temperatures indicated, and ionic radii (IR) of the ions X^{2+}.

X	T (K)	$a(=b)$ (Å)	c (Å)	X-F^I (Å)	X-F^{II} (Å)	IR[a] (Å)
Mg[b]	300	3.9704(8)	13.176(2)	2.005(14)	1.9852(4)	0.72
Zn[b]	300	4.0548(8)	13.096(3)	2.014(16)	2.0274(4)	0.74
Mn[b]	300	4.171(3)	13.259(16)	2.111(15)	2.086(1)	0.83
Mn[c]	4.2	4.151(3)	13.242(10)	2.102(14)	2.076(1)	
Ni[d]	300	4.006	13.076(4)			0.69
Ni[e]	80	3.994	13.04(1)			

[a]R. D. Shannon, Acta Crystallogr. Sect. A 32, 751 (1976).
[b]A. H. M. Schrama, Physica (Utrecht) 68, 279 (1973).
[c]Reference 10.
[d]D. Balz and K. Pleith, Z. Electrochem. 59, 545 (1955).
[e]Reference 6.

transfer of unpaired spins from the second-neighbor Mn to the Mn site adjacent to the F seem to be the major origins of the interactions.[19] For the spin orientation and geometry corresponding to F^I in K_2MnF_4, ENDOR experiments[20,21] yielded a hyperfine constant $B^I + D^I_{10} = -0.067$ MHz/(spin unit) in Mn-doped $KMgF_3$ and $B^I + D^I_{10} = +0.39 \pm 0.03$ MHz/(spin unit) in Mn-doped $KZnF_3$. Apparently, B^I quite strongly depends on the host lattice, and the results in doped $KMgF_3$ and $KZnF_3$ are therefore not at once applicable to K_2MnF_4. In our systems, manifestation of the second-neighbor interactions is however found at the $^{19}F^I$ adjacent to Zn in K_2MnF_4. Ignoring in first instance the difference in the lattice constant a between K_2MnF_4 and $KZnF_3$, i.e., adopting B^I in $KZnF_3$, and accounting for the dipolar field summed over the K_2MnF_4 lattice except for the impurity (230 G), we estimate the hyperfine field at this $^{19}F^I$ to be 1400 ± 110 G for $\langle S_z \rangle = 2.33$. Turning to Fig. 4, where we present data on 0.4- and 0.8-at.% Zn-doped K_2MnF_4 in the region of the nearly-free ^{19}F resonances (mostly $^{19}F^{II}$ resonances), we indeed observe lines near ± 1400 G, more precisely ± 1185 G at $T = 4.2$ K. Apparently, the calculation based on $KZnF_3$:Mn is in good agreement with the experiment, the more so if we note that B^I will be reduced slightly in K_2MnF_4 relative to $KZnF_3$ because of its 4% larger lattice parameter. Another argument that confirms the correctness of the identification is found in the long relaxation time T_1 expected for $^{19}F^I$ associated with a nonmagnetic impurity. In fact, T_1 turned out to be at least two orders of magnitude longer than for a $^{19}F^I$ adjacent to a Mn ion. Further discussion of these resonances is deferred to Sec. V. In a similar way, the resonance of $^{19}F^I$ adjacent to Mg substituted in K_2MnF_4 is calculated at $\pm$ 391 G; these lines have however escaped observation probably because of their closeness to other stronger resonances. The data on 2.2-at.% Mg-doped K_2MnF_4, analogous to Fig. 4, are presented in Fig. 5.

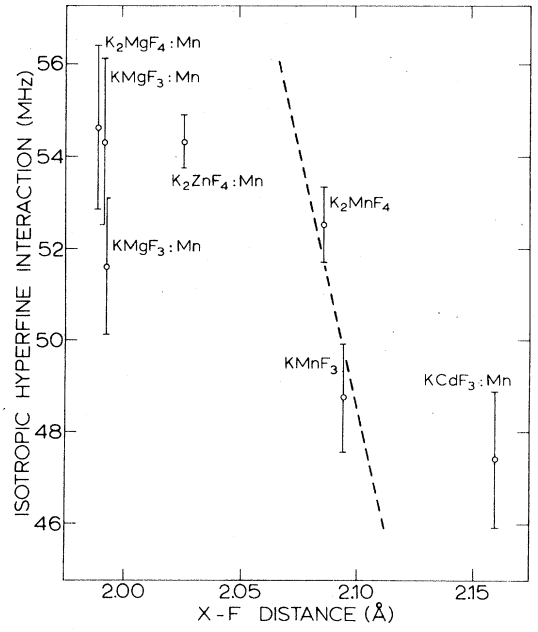

FIG. 3. Isotropic hyperfine interactions A_s in the pure systems K_2MnF_4 and $KMnF_3$, and various related Mn-doped diamagnetic systems KXF_3 (X = Mg, Cd) and K_2XF_4 (X = Mg, Zn) vs X-F distance in the host lattice. For the K_2XF_4 systems the in-layer values are given. The dashed line represents the variation of A_s with X-F as measured by pressure-dependent NMR (Ref. 12).

Direct evidence for local deformation may actually be obtained by comparing the resonance frequency of the $^{19}F^{II}_{(01)}$ intermediate between the impurity and its first Mn neighbors in Zn-doped K_2MnF_4 relative to

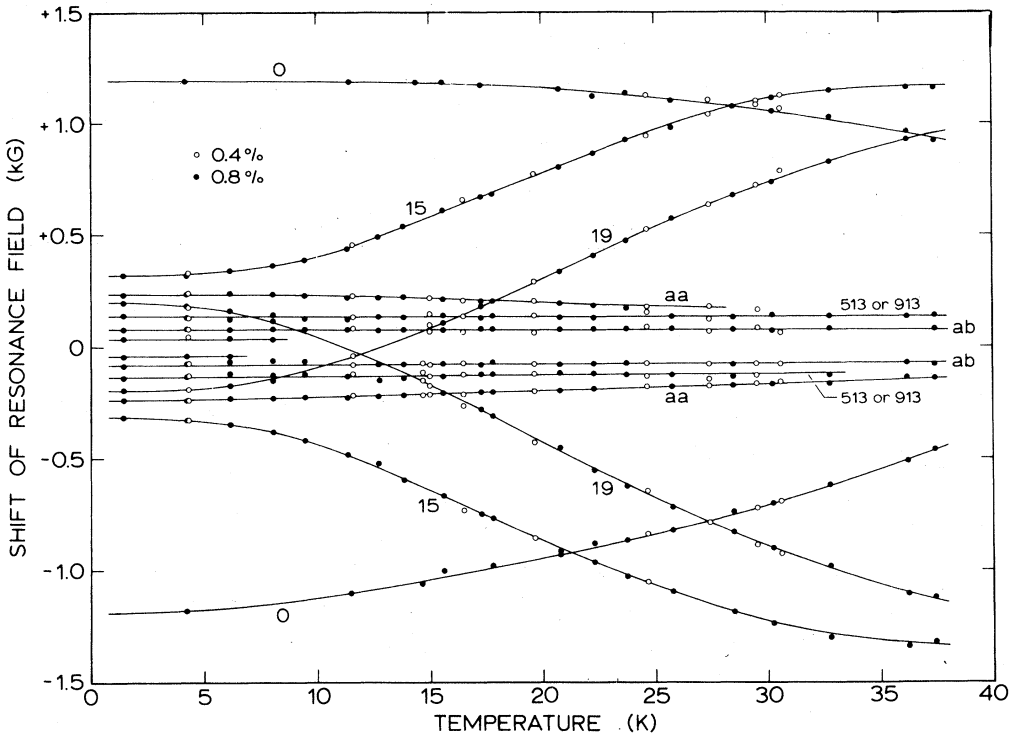

FIG. 4. Nearly-free $^{19}F^{II}$ resonance positions relative to the host resonance in 0.4- and 0.8-at.% Zn-doped K_2MnF_4 vs temperature. The NMR frequency was fixed at 40.000 MHz, corresponding to external fields of about 10 kG. Resonances are labeled according to Fig. 1. For the assignment see Sec. V A. Curves are guides to the eye. The resonances lying at ± 1.19 kG near $T=0$ originate from $^{19}F^{I}$ adjacent to a Zn ion. The figure is symmetric about zero shift because Zn may reside on the up or down sublattice (most of the resonances with positive shift correspond to Zn on the up sublattice); the slight asymmetry is due to effects of local susceptibility and lattice deformation. Shifts of $^{19}F^{II}$ in adjoining layers, produced by dipolar fields only, follow the temperature variation of the host magnetization, as do $^{19}F^{II}$ far away from a Zn ion.

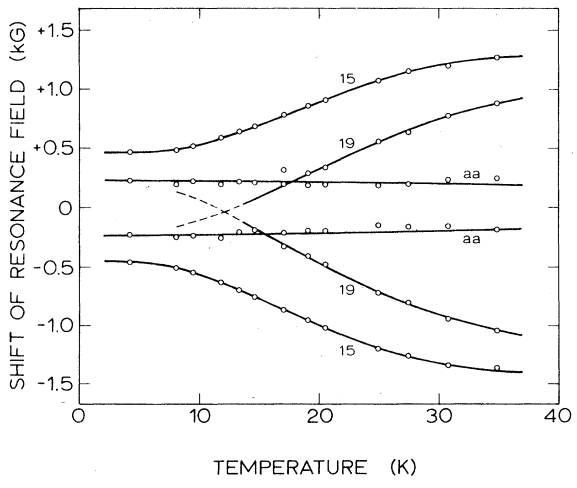

FIG. 5. Same as Fig. 4, but for 2.2-at.% Mg-doped K_2MnF_4.

its Mg-doped counterpart. From the magnetic point of view these substances are of course identical. At zero temperature these frequencies are 103.52 ± 0.03 MHz and 94.95 ± 0.08 MHz, respectively, in vanishing field (the temperature dependence is discussed in Sec. V). Part of the difference of 8.57 MHz is explained by the difference in the second-neighbor contributions from Mn^{2+} at sites 3 and 4. Adopting the B^{II}'s of the diamagnetic systems, similarly to above, we obtain for the second-neighbor hyperfine field originating from these Mn ions, carrying $\langle S_z \rangle = 2.33$, 520 G (0.89 MHz/spin unit) and 220 G (0.38 MHz/spin unit), respectively, yielding a difference of 1.2 MHz. Second-neighbor hyperfine interactions from the other Mn (sites 5, etc.) are not known, but must be very nearly the same for Zn and Mg-doped K_2MnF_4. The balance, 7.4 MHz, is consequently to be attributed to effects of lattice deformation on the first-neighbor hyperfine interaction between $^{19}F^{II}_{(01)}$ and $Mn_{(1)}$. As the lattice parameter a increases in

going from K_2MgF_4 to K_2MnF_4, it is anticipated that in the bond Mg-$F^{II}_{(01)}$-$Mn_{(1)}$ in Mg-doped K_2MgF_4 $F^{II}_{(01)}$ will be displaced away from Mn towards Mg, with a corresponding decrement of the transferred hyperfine interaction relative to the pure system. Similarly, but to a smaller extent, the $Mn_{(1)}$-$F^{II}_{(01)}$ hyperfine interaction in Zn-doped K_2MnF_4 will be reduced. This is indeed reflected in the lower resonance frequency of $^{19}F^{II}_{(01)}$ in the Mg-doped crystal relative to the Zn-doped one. The magnitude of this effect, 7.4 MHz out of ~ 100 MHz, corresponds to a difference of 0.015 Å in the $Mn_{(1)}$-$F^{II}_{(01)}$ separations between the Zn- and Mg-doped crystals. This is about half the difference between the Mg-F^{II} and Zn-F^{II} separations in pure K_2MgF_4 and K_2ZnF_4, respectively.

The case of a Ni impurity in K_2MnF_4 is in many respects very similar. Noting that the lattice parameter a of K_2NiF_4 is 0.17 Å smaller than in K_2MnF_4, we expect considerable shifts of the Ni-$F^{II}_{(01)}$ and $Mn_{(1)}$-$F^{II}_{(01)}$ transferred hyperfine interactions relative to the corresponding pure systems. However, the analysis of the $^{19}F^{II}_{(01)}$ resonance is somewhat more complex than in the case of nonmagnetic impurities because the impurity magnetization adds to the number of unknowns, as do both the direct and second-neighbor hyperfine constants involving the Ni^{2+} ion. Quite direct information on the temperature dependence of the magnetization of the Ni has been deduced from the resonance of $^{19}F^{I}_{(0)}$ adjacent to the impurity itself. Presentation and discussion of these data and those on $^{19}F^{II}_{(0)}$ is deferred to Sec. V, following the calculation of the temperature dependence of the local magnetizations in Sec. IV. The data on $^{19}F^{II}$ associated with the first shells of Mn are given in Fig. 6.

Let us recall at this point that the positions of the weak ^{19}F satellite resonances are a measure of local shifts of the magnetizations, although contaminated with variations of the hyperfine parameters [cf. Eq. (1)]. Here, the in-layer $^{19}F^{II}$, experiencing oppositely aligned transferred hyperfine fields from two Mn^{2+} neighbors, primarily resonate in the external field (Figs. 4–6), as distinct from the out-of-layer $^{19}F^{I}$, for which the hyperfine field predominates the external field. The out-of-layer data for Zn-, Mg- and Ni-doped K_2MnF_4 are presented in Figs. 7–9, respectively. As there are equal numbers of impurities on the up and down sublattices, the $^{19}F^{II}$ resonances will in first instance be symmetric, both in position and amplitude, with respect to the main in-layer reso-

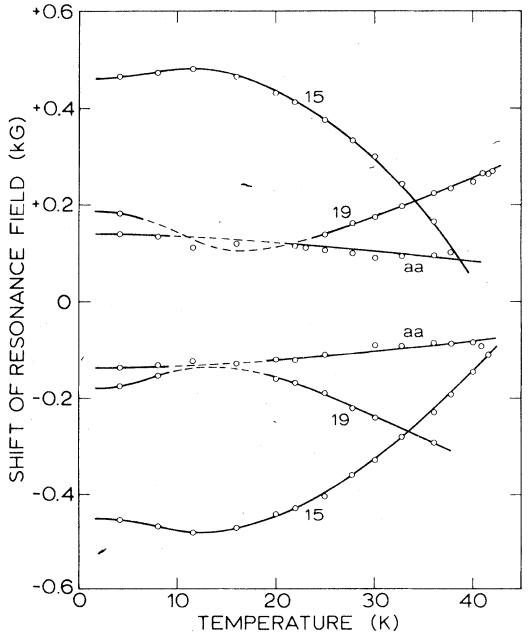

FIG. 6. Same as Fig. 4, but for 2.5-at.% Ni-doped K_2MnF_4.

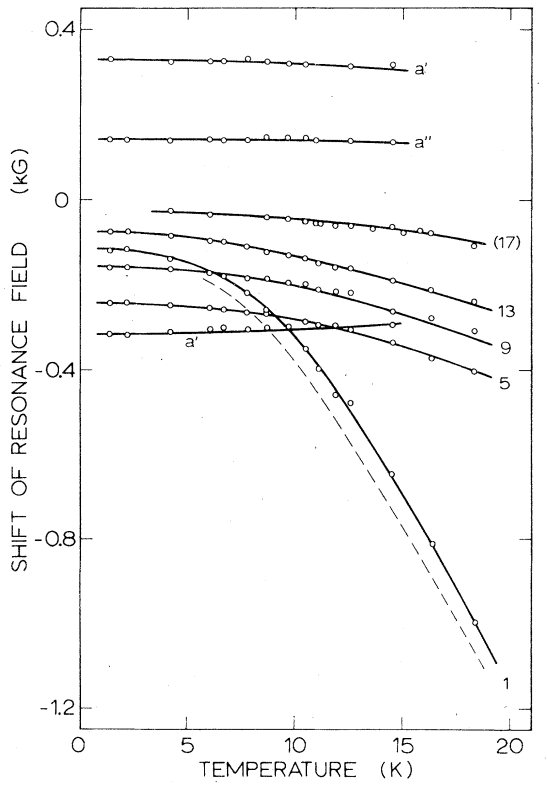

FIG. 7. Resonance positions of out-of-layer $^{19}F^{I}$ relative to the host resonance in 0.4-at.% Zn-doped K_2MnF_4. Labels refer to the $^{19}F^{I}$ positions according to Fig. 1. Identification of resonances labeled 5 and 9 may be subject to interchange (see Sec. V A). Data are taken at low external fields and subsequently interpolated to zero field to eliminate spurious effects of local variation of the susceptibility. The dashed line indicates the $^{19}F^{I}_{(1)}$ position when measured at a fixed frequency of 105.300 MHz at external fields ranging from 8 to 11 kG, depending on temperature.

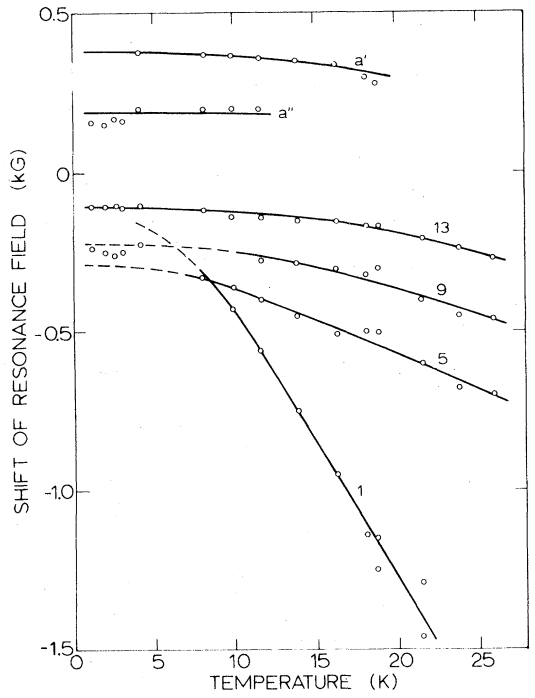

FIG. 8. Resonance positions of out-of-layer $^{19}F^{I}$ in 2.2-at.% Mg-doped K_2MnF_4. As compared to Fig. 7, the linewidth is substantially larger, reducing both resolution and accuracy. Data are taken at 105.300 MHz in external fields between 8 and 11 kG.

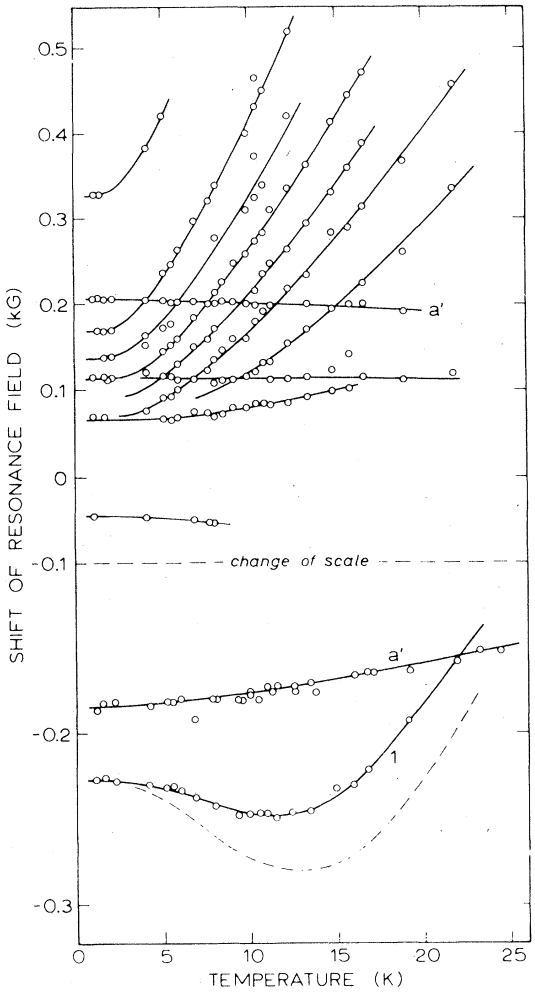

FIG. 9. Resonance positions of out-of-layer $^{19}F^{I}$ in 0.5-at.% Ni-doped K_2MnF_4. Data of the $^{19}F^{I}_{(1)}$ resonances are reduced to zero field, as in Fig. 7. The group of resonances in the upper part of the figure is not related to isolated impurities, but suggests the occurrence of Ni clusters. These resonances prevent the $^{19}F^{I}_{(5)}$ and $^{19}F^{I}_{(9)}$ resonances from being identified. For the dashed line, see caption to Fig. 7.

nance, which arises from $^{19}F^{II}$ at considerable distances from the impurity. However, in a field the $^{19}F^{II}$ resonances are experimentally found to become asymmetrically located towards higher temperatures (cf. Figs. 4–6). The shifts amount to $\sim$ 100 G at 40 K. The temperature dependence of the effect clearly suggests it to be due to the parallel susceptibility $\chi_{\parallel}$ in conjunction with, as we will see shortly, variation of A^{II}. The strongest effects will of course occur for $^{19}F^{II}$ associated with first Mn^{2+} neighbors of the impurity. For the discussion, it is advantageous to break down the impurity-induced deformations at the $^{19}F^{II}$ sites into two independent components, an asymmetric and a symmetric one. In an asymmetric distortion, the $^{19}F^{II}$ is shifted from the midpoint between the two Mn neighbors resulting in an imbalance of the two hyperfine fields. Alternatively, the local magnetizations at the Mn neighbors may have become unequal by virtue of the impurity. By reversing the spins, it is easy to see that an asymmetric distortion will not disturb the symmetry between the $^{19}F^{II}$ resonances associated with up and down impurity sites. The second type of distortion is a symmetric decrease (increase) of the separations between $^{19}F^{II}$ and its first Mn neighbors. Consider the situation in which there is a net hyperfine field at the $^{19}F^{II}$ induced by an external field. The distortion then results, via variation of the hyperfine interaction constants, in an increment (decrement) of the net hyperfine field relative to the far away $^{19}F^{II}$. This effect is clearly proportional to $\chi_{\parallel}$ and independent of the direction of the impurity spin. It shifts a $^{19}F^{II}$ resonance and the one corresponding to the reversed impurity by equal amounts and to the same side, making the NMR spectrum asymmetric. Obviously, these shifts do not contain information of interest on the impurity-induced changes of the magnetizations. For further discussion, we will therefore symmetrize the temperature dependences of the in-layer resonance

fields relative to the main resonance. In this context, we finally remark that in a field asymmetry of the NMR spectrum may also occur, when the local susceptibilities near the impurity are different from that of the host.[22] These effects may again be eliminated by symmetrization.

In order to arrive at shifts of the ^{19}F resonances solely due to impurity-associated changes of the magnetizations, we have to take out the effects associated with lattice deformations, both hyperfine and dipolar. We further wish to remove the spurious shifts originating from second-neighbor hyperfine interactions. As pointed out above, both of these effects are not known quantitatively. By necessity, we therefore have to resort to some kind of heuristic procedure. The underlying idea is to first calculate the line positions at *zero* temperature using *theoretical* local magnetizations and the hyperfine interaction parameters of the *pure* system, and subsequently attribute the departure of the positions so calculated from the experimental zero-temperature line positions to the undesired effects. The procedure is admittedly slightly hybrid in the sense that it is based on the reliability of the Green's-function results, more specifically on the results at low temperatures. Apart from the achievements of Green's functions in calculating the magnetization of the pure system up to say $\frac{1}{2}T_N$, justification is ultimately found in the excellent agreement arrived at for the temperature dependences of the local magnetizations (see Sec. V). In this context, we in particular mention the local magnetizations of the first Mn neighbors of Ni and Zn impurities in K_2MnF_4, as well as the magnetization of the Ni impurity itself.

The out-of-layer $^{19}F^{I}$ could be observed for the first three shells of Mn^{2+} about the impurity. Returning to our example of $^{19}F^{I}_{(1)}$ [cf. Eq. (1)], according to the procedure outlined above the analysis of the shift δf^{I}_{1} proceeds as follows. We first subtract $(A^{I}+D^{I}_{11})\langle \delta S^{z}_{1}(0)\rangle$, as calculated for zero temperature, from the low-temperature shift $\delta f^{I}_{1}(0)$. We note from Eq.(1) that the remainder follows the temperature dependences of the various local magnetizations. To a good approximation, however, the remainder may simply be taken to vary according to $\langle S^{z}_{\infty}\rangle$, the sublattice magnetization of the host lattice. The error made here is indeed quite small, since the departures of $\langle S^{z}_{0}\rangle$ and $\langle S^{z}_{1}\rangle$ from $\langle S^{z}_{\infty}\rangle$ do not exceed 3% up to, say 20 K. The remainder scaled with $\langle S^{z}_{\infty}(T)\rangle$ is then deducted from $\delta f^{I}_{1}(T)$ to yield $(A^{I}+D^{I}_{11})\langle \delta S^{z}_{1}(T)\rangle$, and finally the experimental result for $\langle \delta S^{z}_{1}(T)\rangle$. Similarly, we deduce $\langle \delta S^{z}_{5}(T)\rangle$ for the second shell, etc. The latter quantities, or rather their variation with temperature

$$\Delta S_i(T) = \langle \delta S^{z}_{i}(T)\rangle - \langle \delta S^{z}_{i}(0)\rangle \ , \qquad (2)$$

clearly allow direct comparison with theoretical results on the temperature dependence of the local magnetizations. For the in-layer $^{19}F^{II}$ the procedure is entirely analogous, except for the symmetrization discussed above and the involvement of two Mn^{2+} neighbors (labeled i and j) rather than a single neighbor having direct hyperfine interaction. Accordingly, $\delta f^{II}_{ij}(T)$ is reduced to $\Delta S_i(T)-\Delta S_j(T)$.

As to the magnetization at the Ni impurity itself, the direct- and second-neighbor hyperfine interactions of $^{19}F^{I}_{(0)}$ are not known to sufficient accuracy to allow a precise absolute determination of $\langle S^{z}_{0}(T)\rangle$. In contrast to the various shells of Mn neighbors, however, we are here not interested in minute changes of the NMR frequencies relative to the host. When the minor effects of the first shell of Mn^{2+} due to second-neighbor hyperfine interaction are taken to scale with the impurity magnetization, f^{I}_{0} is a direct measure of the temperature dependence of $\langle S^{z}_{0}(T)\rangle$. For $^{19}F^{II}_{(01)}$ adjacent to a nonmagnetic impurity the situation is quite similar. Here, we find $\Delta S_1(T)/\langle S^{z}_{1}(0)\rangle$, virtually equal to $\Delta S_1(T)/\langle S^{z}_{\infty}(0)\rangle$, directly from the decrement of f^{II}_{01} with temperature relative to f^{II}_{01} at zero temperature. Evidently, this alternative determination of $\Delta S_1(T)$, which is *independent* of the result of the analysis of the f^{I}_{1} resonance, provides a useful check on our analysis. Finally, the resonance of $^{19}F^{I}_{(0)}$ adjacent to Zn is processed in a similar way to obtain $\Delta S_1(T)$, after symmetrization of the data and accounting for the dipolar field. The latter determination of $\Delta S_1(T)$ has of course a large error because of the smallness of second-neighbor hyperfine interaction.

III. THEORY

In this section we develop a Green's-function formalism appropriate for calculating magnetizations in 2-D antiferromagnets, both the pure systems and systems in which a single magnetic ion is replaced by an impurity. Generally, the equations of motion of Green's functions contain Green's functions of higher order. Solution of these equations is intractable, unless some sort of random-phase approximation (RPA) is applied[2,3] to break the higher-order Green's functions down to lower-order ones. As the impurity problem is of local nature, we will employ a procedure in which products of the operators of the *local* spin deviations are decoupled. With local decoupling, the Hamiltonian up to order $1/2S$, i.e., the part containing up to four-operator terms in the spin deviations, will appear to reduce to a simple two-operator form, which makes the equations of motion solvable without decoupling of the Green's functions.

A. Pure systems

Before discussing the impurity problem, we first apply local decoupling to the case of the pure system, and verify that the results up to order $1/2S$ are in accordance with the usual Oguchi energy renormalization.[23] For a two-sublattice antiferromagnet ordered along the c axis the Hamiltonian may be written as

$$\mathcal{H}_{\text{pure}} = |J| \sum_{\langle l,m \rangle} \vec{S}_l \cdot \vec{S}_m - g\mu_B H_A \sum_l S_l^z + g\mu_B H_A \sum_m S_m^z \ , \tag{3}$$

where the staggered field H_A represents the anisotropy. For K_2MnF_4,[7] $J = -8.41 \pm 0.06$ K, while $\alpha = g\mu_B H_A / z|J|S = 0.0038$ at $T = 0$, with z the number of nearest neighbors. The summation involving the exchange interaction J is restricted to nearest-neighbor pairs $\vec{S}_l$ and $\vec{S}_m$, situated on the up and down sublattices, respectively. After the Holstein-Primakoff transformation

$$\begin{aligned} S_l^+ &= [2S_l(1 - a_l^\dagger a_l/2S_l)]^{1/2} a_l \ , \\ S_m^+ &= b_m^\dagger [2S_m(1 - b_m^\dagger b_m/2S_m)]^{1/2} \ , \\ S_l^- &= a_l^\dagger [2S_l(1 - a_l^\dagger a_l/2S_l)]^{1/2} \ , \\ S_m^- &= [2S_m(1 - b_m^\dagger b_m/2S_m)]^{1/2} b_m \ , \\ S_l^z &= S_l - a_l^\dagger a_l, \quad S_m^z = -S_m + b_m^\dagger b_m \ , \end{aligned} \tag{4}$$

we distinguish, up to order $1/2S$, two- and four-operator terms in the Hamiltonian (for later use in the impurity case we have attached site labels to the spins; in the pure system $S_l = S_m = S$). The two-operator part, $\mathcal{H}_0$, reads

$$\mathcal{H}_0 = |J|S \sum_{\langle l,m \rangle} [(1+\alpha)(a_l^\dagger a_l + b_m^\dagger b_m) + a_l b_m + a_l^\dagger b_m^\dagger] \ . \tag{5}$$

The four-operator part, $\mathcal{H}_1$, is given by

$$\mathcal{H}_1 = -\frac{|J|S}{4S} \sum_{\langle l,m \rangle} (a_l^\dagger a_l a_l b_m + a_l b_m^\dagger b_m b_m + b_m^\dagger a_l^\dagger a_l^\dagger a_l + b_m^\dagger b_m^\dagger b_m a_l^\dagger + 4 a_l^\dagger a_l b_m^\dagger b_m) \ . \tag{6}$$

The standard way to proceed from Eq. (5) is to introduce sets of spin waves on the up and down sublattices,

$$a_{\vec{k}} = N^{-1/2} \sum_l a_l e^{i\vec{k}\cdot\vec{r}_l} \ , \quad b_{\vec{k}}^\dagger = N^{-1/2} \sum_m b_m^\dagger e^{i\vec{k}\cdot\vec{r}_m} \ , \tag{7}$$

and to diagonalize the result by the Bogoliubov transformation

$$\alpha_{\vec{k}} = u_{\vec{k}} a_{\vec{k}} + v_{\vec{k}} b_{\vec{k}}^\dagger, \quad \beta_{\vec{k}} = v_{\vec{k}} a_{\vec{k}}^\dagger + u_{\vec{k}} b_{\vec{k}} \tag{8}$$

to normal modes $\alpha_{\vec{k}}$ and $\beta_{\vec{k}}$. For the renormalization corrections,[23] Eqs. (7) and (8) are subsequently applied to Eq. (6) followed by decoupling in $\vec{k}$ space. Since both the transformations, Eqs. (7) and (8), are linear, however, the decoupling may be done directly in Eq. (6), i.e., the decoupling is applied to the local spin deviations prior to the transformations. The statement is proved by writing out the general form of the decoupling of a four-operator term,

$$\begin{aligned} abcd \rightarrow\ & ab\langle cd \rangle + ac\langle bd \rangle + ad\langle bc \rangle \\ & + bc\langle ad \rangle + bd\langle ac \rangle + cd\langle ab \rangle \ , \end{aligned} \tag{9}$$

for local spin deviations, applying Eqs. (7) and (8), and finally decoupling of the left-hand side. The operator combinations $a_l b_m^\dagger, a_l a_l$, and $b_m^\dagger b_m^\dagger$ do not contribute because they are off-diagonal after the transformations. For the first term in $\mathcal{H}_1$, e.g., we may accordingly set

$$a_l^\dagger a_l a_l b_m = 2 a_l^\dagger a_l \langle a_l b_m \rangle + 2 a_l b_m \langle a_l^\dagger a_l \rangle \ . \tag{10}$$

Introducing $\Delta = \langle a_l^\dagger a_l \rangle = \langle b_m^\dagger b_m \rangle$ for the number of spin deviations on the up or down sublattice, and defining $\mu = \langle a_l b_m \rangle$ to describe the correlation between neighboring spins (note that in the pure systems $\langle a_l^\dagger a_l \rangle$, etc. are independent of the location), we find the *effective* two-operator Hamiltonian in local spin deviations

$$\mathcal{H}_{\text{pure}} = |J|SR \sum_{\langle l,m \rangle} [(1 + \alpha/R)(a_l^\dagger a_l + b_m^\dagger b_m) + a_l b_m + a_l^\dagger b_m^\dagger] \ , \tag{11}$$

in which the renormalization is contained in

$$R = 1 - (\Delta + \mu)/S \ . \tag{12}$$

As Eq. (5), Eq. (11) may be diagonalized with Eqs. (7) and (8), yielding the dispersion relation

$$E_{\vec{k}} = z|J|SR[(1 + \alpha/R)^2 - \gamma_{\vec{k}}^2]^{1/2} \ . \tag{13}$$

Here, $\gamma_{\vec{k}} = z^{-1} \sum_{\vec{\delta}} e^{i\vec{k}\cdot\vec{\delta}}$ is a geometrical factor, with $\vec{\delta}$ denoting a nearest-neighbor displacement in the quadratic layer. The Bogoliubov coefficients are however slightly modified compared to diagonalization of Eq. (5) to become

$$u_{\vec{k}} = [\tfrac{1}{2}(G_{\vec{k}} + 1)]^{1/2}, \quad v_{\vec{k}} = [\tfrac{1}{2}(G_{\vec{k}} - 1)]^{1/2} \ , \tag{14}$$

with

$$G_{\vec{k}} = (1 + \alpha/R)/[(1 + \alpha/R)^2 - \gamma_{\vec{k}}^2]^{1/2} \ . \tag{15}$$

In the calculations Δ, μ, and R are needed in terms of spin waves. With

$$n_{\vec{k}} = \langle \alpha_{\vec{k}}^\dagger \alpha_{\vec{k}} \rangle = \langle \beta_{\vec{k}}^\dagger \beta_{\vec{k}} \rangle = [\exp(E_{\vec{k}}/k_B T) - 1]^{-1} \ ,$$

we have

$$\Delta = N^{-1} \sum_{\vec{k}} [(u_{\vec{k}}^2 + v_{\vec{k}}^2) n_{\vec{k}} + v_{\vec{k}}^2] \quad , \tag{16}$$

$$\mu = N^{-1} \sum_{\vec{k}} \gamma_{\vec{k}} (-2u_{\vec{k}} v_{\vec{k}}) (n_{\vec{k}} + \tfrac{1}{2}) \quad , \tag{17}$$

which substituted in Eq. (12) give R. With Eqs. (16) and (17) it is straightforward to show that up to order $1/2S$ Eq. (13) is indeed identical to Oguchi's first-order renormalized dispersion.[7]

B. Impure systems

We consider a quadratic-layer antiferromagnet with an impurity located on, say, the up sublattice. Extreme dilution is implied so that the impurities have no interactions with each other. The effective two-magnon Hamiltonian of the pure system, Eq. (11), is then augmented with a local perturbation. That is, taking the origin at the impurity,

$$\mathcal{H} = \mathcal{H}_{\text{pure}} + V \quad , \tag{18}$$

$$V = (|J_0| \sum_{\vec{\delta}} \vec{S}_0 \cdot \vec{S}_{\vec{\delta}} - g_0 \mu_B H_{A0} S_0^z) - (|J| \sum_{\vec{\delta}} \vec{S} \cdot \vec{S}_{\vec{\delta}} - g \mu_B H_A S^z) \quad , \tag{19}$$

where the constant J_0 describes the exchange interaction between the impurity spin $\vec{S}_0$ and its z nearest-neighbor spins $\vec{S}_{\vec{\delta}}$; g_0 and H_{A0} are the local g factor and anisotropy at the impurity site, respectively. Further modifications of the system than those included in Eq. (19), notably in the exchange parameters between the first and second shells of neighbors, are ignored. Applying on the spin operators in Eq. (19) the Holstein-Primakoff transformation, Eq. (4), and evaluating the result up to order $1/2S$, we obtain terms containing two and four local spin-deviation operators. After decoupling of the latter according to Eq. (10), we find for the perturbation the *effectively renormalized* two-operator form

$$\frac{V}{z|J|SR} = \tau a_0^\dagger a_0 + \sigma \sum_{\vec{\delta}} b_{\vec{\delta}}^\dagger b_{\vec{\delta}} + \frac{\lambda}{z} \sum_{\vec{\delta}} (a_0 b_{\vec{\delta}} + a_0^\dagger b_{\vec{\delta}}^\dagger) \quad , \tag{20}$$

with

$$\tau = \frac{1}{R} \left[\alpha_0 - \alpha + \frac{|J_0|}{|J|} - 1 - \left(\frac{|J_0| \langle a_0 b_{\vec{\delta}} \rangle}{|J| (S_0 S)^{1/2}} - \frac{\mu}{S} \right) - \left(\frac{|J_0| \langle b_{\vec{\delta}}^\dagger b_{\vec{\delta}} \rangle}{|J| S} - \frac{\Delta}{S} \right) \right] \quad , \tag{21}$$

$$\sigma = \frac{1}{z|J|SR} \{ (|J_0| S_0 - |J| S) - [|J_0| (S_0/S)^{1/2} \langle a_0 b_{\vec{\delta}} \rangle - |J| \mu] - (|J_0| \langle a_0^\dagger a_0 \rangle - |J| \Delta) \} \quad , \tag{22}$$

$$\lambda = \frac{1}{|J|SR} \{ [|J_0| (S_0 S)^{1/2} - JS] - \tfrac{1}{2} [|J_0| (S/S_0)^{1/2} \langle a_0^\dagger a_0 \rangle - |J| \Delta] - \tfrac{1}{2} [|J_0| (S_0/S)^{1/2} \langle b_{\vec{\delta}}^\dagger b_{\vec{\delta}} \rangle - |J| \Delta] - (|J_0| \langle a_0 b_{\vec{\delta}} \rangle - |J| \mu) \} \quad . \tag{23}$$

Here, $\alpha_0 = g_0 \mu_B H_{A0} / z|J|S$. With R, Δ, and μ of the pure host lattice it is easily verified that V vanishes in the pure system.

In order to calculate the thermal averages of the S_j^z, situated at the various positions j about the impurity, we make use of the retarded Green's functions defined by

$$G_{AB}(t) = -i\Theta(t) \langle [A(t), B(0)] \rangle \quad , \tag{24}$$

where $\Theta(t)$ is the unit step function, A and B are local spin-deviation operators, given in Heisenberg notation, and the angular brackets denote the thermodynamic ensemble average of the expectation value of the operator within; the square brackets indicate a commutator. As Green's-functions techniques are extensively discussed in the literature, we confine ourselves to briefly indicating the notations used. The time Fourier transform is defined by

$$G_{AB}(E) = \int_{-\infty}^{+\infty} G_{AB}(t) e^{+iEt} dt \quad , \tag{25}$$

and its equation of motion reads

$$E G_{AB}(E) = \langle [A, B] \rangle + G_{[A, \mathcal{H}], B}(E) \quad . \tag{26}$$

Evaluating the time integral Eq. (25) involving $\Theta(t)$, we have

$$G_{AB}(E) = \int (e^{+\beta E'} - 1) \mathcal{A}_{BA}(E') \frac{dE'}{E - E' + i0^+} \quad , \tag{27}$$

in which the spectral weight function $\mathcal{A}_{BA}(E)$ is defined by

$$\mathcal{A}_{BA}(E) = \frac{1}{Z} \sum_{\alpha, \gamma} e^{-\beta E_\gamma} \langle \gamma | B | \alpha \rangle \langle \alpha | A | \gamma \rangle \delta(E_\gamma - E_\alpha - E) \quad , \tag{28}$$

with Z the partition function, β the inverse temperature, and α and γ representing exact eigenstates of the system. Integrating $\mathfrak{a}_{BA}(E)$ over the energy would directly give $\langle BA\rangle$, but $\langle BA\rangle$ is more conveniently recovered from the imaginary part of the Green's function,

$$\langle BA\rangle = -\int \frac{dE}{e^{\beta E}-1}\frac{\mathrm{Im}G_{AB}(E)}{\pi} \quad . \tag{29}$$

Equation (29) may be evaluated without detailed knowledge of the exact eigenfunctions. It is noted that Eq. (29) holds provided $\mathfrak{a}_{BA}(E)$ is real, which is the case when using the Holstein-Primakoff formalism. There are no contributions to $\mathrm{Im}G_{AB}(E)$ other than from the poles of $G_{AB}(E)$. On the other hand, if Dyson-Maleev had been used, $\mathfrak{a}_{BA}(E)$ would generally have given undesired contributions to $\mathrm{Im}G_{AB}(E)$. Integrating the imaginary part of the Green's function, Eq. (27), and using the relation $\mathfrak{a}_{AB}(E)=e^{\beta E}\mathfrak{a}_{BA}(E)$, we have

$$-\frac{1}{\pi}\int \mathrm{Im}G_{AB}(E)\,dE = \langle [A,B]\rangle \quad , \tag{30}$$

which may provide a useful check on the numerical evaluation of $\mathrm{Im}G_{AB}(E)$, as we will see below.

Generally $G_{[A,\mathcal{H}],B}(E)$ occurring in the equation of motion, Eq. (26), contains Green's functions of higher order, which require some kind of decoupling to lower-order Green's functions. However, in our scheme decoupling has already been done in the Hamiltonian resulting in effective quadratic forms [cf. Eqs. (11) and (20)]. Then, $G_{A,B}(E)$ and $G_{[A,\mathcal{H}],B}(E)$ are of the same order in the local-spin-deviation operators, rendering decoupling of the Green's functions unnecessary. For a set of Green's functions that couple with each other, we take a_l or $b_m^\dagger$ as the first operator in $G_{AB}(E)$ in combination with their conjugates $a_l^\dagger$ or b_m as second operator. For convenience, we henceforth label Green's functions according to the lattice sites of the operators, i.e., G_{ll}, G_{lm}, G_{ml}, and G_{mm}. We further introduce dimensionless energies $\epsilon = E/z|J|SR$, and dimensionless Green's functions

$$\Gamma_{ij}(\epsilon) = z|J|SRg_jG_{ij}(E) \quad , \tag{31}$$

where the site labels i and j may refer to both up and down sublattice sites; $g_j=1$ or -1 for j on the up or down sublattice, respectively (g_j is introduced anticipatorily to arrive at a simple matrix form of the equation of motion). Working out the commutators of a_l and $b_m^\dagger$ with the Hamiltonian, the equations of motion of the Green's functions with the first operator at an up site l read

$$(\epsilon-1-\alpha/R)\Gamma_{lj}-\frac{1}{z}\sum_{m(l)}\Gamma_{mj} = g_j\delta_{l,j}+\delta_{l,0}\left[\tau\Gamma_{0j}+\frac{\lambda}{z}\sum_{m(0)}\Gamma_{mj}\right] \quad . \tag{32}$$

Here, nearest-neighbor positions of l at the other sublattice are denoted by $m(l)$. Similarly, for the first operator at a down site

$$(\epsilon+1+\alpha/R)\Gamma_{mj}+\frac{1}{z}\sum_{l(m)}\Gamma_{lj} = -g_j\delta_{m,j}-\sum_{l(m)}\delta_{l,0}\left[\sigma\Gamma_{mj}+\frac{\lambda}{z}\Gamma_{0j}\right] \quad . \tag{33}$$

For the pure crystals, the solutions Γ_{ij}^0 of the Green's functions can, after Fourier transformation by

$$\Gamma_{ij}=\sum_{\vec{k}}\Gamma_{\vec{k}}\exp[i\vec{k}\cdot(\vec{r}_i-\vec{r}_j)] \quad , \tag{34}$$

be expressed in the functions

$$U(\epsilon,\vec{p})=\frac{1}{N}\lim_{s\to 0^+}\sum_{\vec{k}}\frac{e^{i\vec{k}\cdot\vec{p}}}{(\epsilon+is)^2-(1+\alpha/R)^2+\gamma_{\vec{k}}^2} \quad , \tag{35}$$

$$V(\epsilon,\vec{p})=\frac{1}{N}\lim_{s\to 0^+}\sum_{\vec{k}}\frac{\gamma_{\vec{k}}e^{i\vec{k}\cdot\vec{p}}}{(\epsilon+is)^2-(1+\alpha/R)^2+\gamma_{\vec{k}}^2} \quad , \tag{36}$$

with $\vec{p}=\vec{r}_i-\vec{r}_j$. From the $2N\times 2N$ matrix Γ^0, partitioned by sublattices, the first $(z+1)\times(z+1)$ part is then formally represented by

$$\Gamma^0=\begin{pmatrix}(\epsilon+1+\alpha/R)U(\epsilon,\vec{0}) & V(\epsilon,\vec{\delta})\Delta \\ -V(\epsilon,-\vec{\delta})\Delta & (\epsilon-1-\alpha/R)U(\epsilon,\vec{p})\Delta'\end{pmatrix} \quad , \tag{37}$$

where Δ and Δ' are 1×4 and 4×4 matrices, respectively, with all elements unity. The functions U and V have poles for $\epsilon^2=(1+\alpha/R)^2-\gamma_{\vec{k}}^2$, i.e., the spin-wave dispersion of the two-dimensional antiferromagnet [cf. Eq. (13)]. The numerical evaluation of U and V, which are of elementary importance in the impurity problem, will be discussed in Sec. IV.

By analogy with Walker *et al.*[2] we write the equations of motion Eqs.(32) and (33) in the matrix form (Generally I denotes an identity matrix of appropriate dimension)

$$M\Gamma = I + V\Gamma \quad . \tag{38}$$

Here, M, a $2N\times 2N$ matrix of which the first $(z+1)\times(z+1)$ part is represented by

$$M=\begin{pmatrix}\epsilon-1-\alpha/R & -\frac{1}{4}\Delta \\ \frac{1}{4}\Delta & (\epsilon+1+\alpha/R)I\end{pmatrix} \quad , \tag{39}$$

describes the pure crystal; the perturbation V is restricted to the interaction of the impurity with its nearest neighbors, and accordingly represented by the $(z+1)\times(z+1)$ matrix

$$V=\begin{pmatrix}\tau & (\lambda/z)\Delta \\ -(\lambda/z)\Delta & -\sigma I\end{pmatrix} \quad . \tag{40}$$

Substituting in Eq. (38) the solution for the pure lat-

tice, $\Gamma^0 = M^{-1}$, we have $\Gamma = \Gamma^0 + \Gamma^0 V \Gamma$, which may be rewritten to the formal solution

$$\Gamma = (I - \Gamma^0 V)^{-1} \Gamma^0 \ . \tag{41}$$

In our calculations (Sec. IV B) we will include the first three shells of Mn neighbors about the impurity. The labeling of the 13 Mn sites involved is given in Fig. 1. This requires extending the matrix Γ^0 as given in Eq. (37) to 13×13 elements, which is straightforward and will not be reproduced here; extension of the perturbation matrix V simply amounts to adding zeros. Analytic inversion of the matrix $I - \Gamma^0 V$, now also having dimension 13×13, is a major calculational task. Making use of the symmetry properties of the magnetic structure (group D_{4h}) to transform the matrix to block-diagonal form,[24] we find four s modes, six p modes, which are two-fold degenerate, and three d modes. The transformation matrix is

$$S = \begin{pmatrix}
1 & & & & & & & & & & & & \\
 & a & & & b & & & & & & a & & \\
 & a & & & -b & & & & & & a & & \\
 & a & & & & & b & & & & -a & & \\
 & a & & & & & -b & & & & -a & & \\
 & & a & -a & & & a & & a & & & & \\
 & & a & a & & & -a & & a & & & & \\
 & & a & a & & & a & & -a & & & & \\
 & & a & -a & & & -a & & -a & & & & \\
 & & & a & & b & & & & & & a & \\
 & & & a & & -b & & & & & & a & \\
 & & & a & & & & b & & & & -a & \\
 & & & a & & & & -b & & & & -a &
\end{pmatrix} , \tag{42}$$

with $a = \frac{1}{2}$ and $b = \frac{1}{2}\sqrt{2}$. The inversion of the 13×13 matrix $I\text{-}\Gamma^0 V$ is now reduced to inversion of the s, p, and d submatrices occurring at the diagonal of the matrix $I - (S^{-1}\Gamma^0 S)(S^{-1} V S)$. It appears that the d submatrix can be partitioned further into a single element and a 2×2 matrix. Accordingly, the determinant of the matrix $I - \Gamma^0 V$ is written

$$D(\epsilon) = D_s D_p D_{d1} D_{d2} \ . \tag{43}$$

Explicit expressions of the submatrices, function of the energy ϵ, are

$$\begin{aligned}
D_s &= 1 + 4\sigma(\epsilon - 1 - \alpha/R - \tau) + \lambda(\lambda + 2) - \{\tau + (\epsilon - 1 - \alpha/R)[4\sigma(\epsilon - 1 - \alpha/R - \tau) \\
&\qquad + \lambda(\lambda + 2)]\}(\epsilon + 1 + \alpha/R)\, U(00) \ , \\
D_p &= 1 + \sigma(\epsilon - 1 - \alpha/R)[U(00) - U(11)] \ , \\
D_{d1} &= 1 \ , \\
D_{d2} &= 1 + \sigma(\epsilon - 1 - \alpha/R)[U(00) + U(11) - 2U(10)] \ .
\end{aligned} \tag{44}$$

Here, we have introduced an alternative notation for $U(\epsilon, \vec{p})$ and $V(\epsilon, \vec{p})$ by omitting the energy argument ϵ and expressing $\vec{p}$ in vectors $\vec{v}$ and $\vec{w}$ spanning the quadratic *magnetic* unit cell, i.e., $U(lm) = U(\epsilon, l\vec{v} + m\vec{w})$ with l and m integer or half integer. From evaluation of Eq. (41) the Green's functions necessary to calculate the magnetization at the impurity and the three shells of Mn are then found to be

$$\Gamma_{00}=\{4\sigma+[1-4\sigma(\epsilon-1-\alpha/R)](\epsilon+1+\alpha/R)U(00)\}/D_s \ ,$$

$$\Gamma_{01}=-\Gamma_{10}=(1+\lambda)V(\tfrac{1}{2}\tfrac{1}{2})/D_s \ ,$$

$$\Gamma_{11}=(\epsilon-1-\alpha/R-\tau)V(\tfrac{1}{2}\tfrac{1}{2})/D_s+(\epsilon-1-\alpha/R)[U(00)-U(11)]/2D_p$$
$$+(\epsilon-1-\alpha/R)[U(00)+U(11)-2U(10)]/4D_{d2} \ ,$$

$$\Gamma_{55}=(\epsilon+1+\alpha/R)U(00)+[(\epsilon+1+\alpha/R)U(10)]^2 \qquad (45)$$
$$\times[2\lambda(\epsilon-1-\alpha/R)+\tau+4\sigma(\epsilon-1-\alpha/R-\tau)(\epsilon-1-\alpha/R)]/D_s+\sigma[V(\tfrac{1}{2}\tfrac{1}{2})-V(\tfrac{3}{2}\tfrac{1}{2})]^2/D_p \ ,$$

$$\Gamma_{99}=(\epsilon+1+\alpha/R)U(00)+[(\epsilon+1+\alpha/R)U(11)]^2$$
$$\times[2\lambda(\epsilon-1-\alpha/R)+\tau+4\sigma(\epsilon-1-\alpha/R-\tau)(\epsilon-1-\alpha/R)]/D_s+\sigma[V(\tfrac{1}{2}\tfrac{1}{2})-V(\tfrac{3}{2}\tfrac{3}{2})]^2/2D_p$$
$$+\sigma[V(\tfrac{1}{2}\tfrac{1}{2})-2V(\tfrac{3}{2}\tfrac{1}{2})+V(\tfrac{3}{2}\tfrac{3}{2})]^2/4D_{d2} \ .$$

It is noted that in the expressions for Γ_{55} and Γ_{99} the perturbation is additive to the pure system, which is contained in the first terms.

Equations (45) are the final Green's-function results from which the local magnetizations at the impurity (site 0) and first three shells (at representative sites 1, 5, and 9) can be calculated by use of the equivalent of Eq. (29), which reads

$$\langle BA\rangle=-\frac{g_j}{\pi}\int\frac{d\epsilon}{e^{z|J|SR\beta\epsilon}-1}\mathrm{Im}\Gamma_{AB} \ , \qquad (46)$$

with g_j referring to operator B. In the calculations, the expectation values occurring in the perturbation parameters τ, σ, and λ, as well as those in the renormalization R, are to be taken care of by iterating the numerical process until self-consistency is reached.

C. Other theories

In the literature, other Green's-function approaches have been reported on the problem of the local magnetization about a substitutional impurity in an antiferromagnet. A very profound treatment has been published by Walker *et al.*,[2] based on the Green's functions of local *spin* operators S^+ and S^-. In the subsequent quantitative analysis the emphasis was on a 3-D system, notably the body-centered antiferromagnet MnF_2, with overall good results. The RPA chosen by them has however the shortcoming, which they themselves point out, of not taking into account the angle that the impurity makes with its neighbors. It is of interest to discuss this in some detail in relation to the decoupling scheme used here. Walker *et al.* adopt a decoupling scheme within the Green's functions, in which the approximations are of the form

$$S_l^zS_m^+\rightarrow\langle S_l^z\rangle S_m^+ \ . \qquad (47)$$

In our approach based on local magnon operators decoupling is done in the four-magnon part of the Hamiltonian and decoupling of the Green's functions is unnecessary. For the sake of comparison only, we however apply our decoupling to $S_l^zS_m^+$ after transformation to magnon variables. This yields in first order

$$(S-a_l^\dagger a_l)b_m^\dagger\rightarrow(S-\langle a_l^\dagger a_l\rangle)b_m^\dagger-\langle a_l^\dagger b_m^\dagger\rangle a_l \ , \qquad (48)$$

which, after transformation back to spin operators, contains the term $\langle S_l^-S_m^+\rangle S_l^+$, not present in Eq. (47) and involving the phase between the nearest neighbors l and m. Apart from the technicalities associated with decoupling in the Hamiltonian instead of the Green's functions, we may therefore say that our treatment goes beyond that of Walker *et al.* in that correlations in the transverse components of neighboring spins are taken into account.

The decoupling used clearly also bears on the way the spin-wave energy is renormalized by dynamical interactions. Quite generally, renormalization is dependent on temperature, and so are its effects on thermodynamic properties such as the magnetization. In our treatment, renormalization is given by the factor [cf. Eq. (12)]

$$R=1-(\langle a_l^\dagger a_l\rangle+\langle a_lb_m\rangle)/S \ , \qquad (49)$$

which, as discussed in connection with Eq. (13), is indistinguishable from renormalization in the conventional Oguchi renormalized spin-wave theory. Similarly to the latter, the present approach gives excellent fits to NMR data on the sublattice magnetization up to $\sim\frac{1}{2}T_N$. In the formalism of Walker *et al.* the energy is renormalized according to the magnetization, corresponding to a renormalization factor

$$R'=1-\langle a_l^\dagger a_l\rangle/S \ . \qquad (50)$$

With respect to Eq. (49), this again amounts to deletion of the nearest-neighbor phase relationship. Because R' gives too strong a renormalization, the ther-

mal excitation of spin waves will be overestimated. As a result the decoupling by Walker *et al.* predicts too rapid a decrease of the local magnetizations (as well as the magnetization in pure systems). It must however be observed that the effect of omitting the phase relationship is less serious in 3-D antiferromagnets, than it is in the 2-D ones. This will be emphasized in Sec.V below, where we have reworked the formalism of Walker *et al.* for the quadratic layer. Numerical results for the pure system and the first three shells of Mn^{2+} ions in impure systems will be compared with our results.

Still another theory has been published by Waterai and Kawasaki.[3] These authors restricted themselves to modifications of the magnetizations on the impurity and the first shell of neighbors. Their treatment is based on Dyson-Maleev spin waves. The decoupling employed is local and includes the correlations between nearest-neighbors, as in the present paper, but with the noteworthy difference that it is applied to higher-order Green's functions to linearize the equations of motion, instead of the Hamiltonian. After correction for the nonphysical aspects due to the use of Dyson-Maleev spin waves, the differences with our treatment are however of order higher than $1/2S$. Consequently, Waterai and Kawasaki's treatment adapted to the square lattice and extended to three shells of neighbors would bring forth local magnetizations that are indistinguishable from our results. To check our calculations, we evaluated[25] the expressions given by Waterai and Kawasaki for the magnetization at the impurity and the first shell in a separate computation, yielding identical results.

IV. NUMERICAL EVALUATION

A. Green's functions of pure system

The evaluation of the elementary Green's functions U and V in a 2-D quadratic antiferromagnet closely follows the treatment given by Walker, Cetlin, and Hone[26] for the 3-D bcc structure. Hence, we will only give a concise treatment of the characteristic features.

Replacing in Eq. (35) the summation by an integral we have

$$U(\epsilon,\vec{p})=\frac{1}{(2\pi)^2}\lim_{s\to 0^+}\int_{-\pi}^{+\pi}d\phi_1\int_{-\pi}^{+\pi}d\phi_2\frac{\exp(i\vec{p}\cdot\vec{\phi})}{(\epsilon+is)^2-(1+\alpha/R)^2+\cos^2\frac{1}{2}\phi_1\cos^2\frac{1}{2}\phi_2}\ , \tag{51}$$

where we have substituted $\gamma_{\vec{k}}=\cos(\frac{1}{2}k_xa)\times\cos(\frac{1}{2}k_ya)$, with a the distance between neighbors in a sublattice; for convenience $\phi_1=k_xa$ and $\phi_2=k_ya$. It is not necessary to separately calculate $V(\epsilon,\vec{p})$, as V may be extracted from the U's with the relation

$$V(\epsilon,\vec{p})=\frac{1}{z}\sum_{\vec{\delta}}U(\epsilon,\vec{p}+\vec{\delta})\ . \tag{52}$$

Another relation between U and V is

$$[\epsilon^2-(1+\alpha/R)^2]U(\epsilon,\vec{p})=\delta(\vec{p})-\frac{1}{z}\sum_{\vec{\delta}}V(\epsilon,\vec{p}+\vec{\delta})\ . \tag{53}$$

Eliminating V from Eqs. (52) and (53) we have

$$[\epsilon^2-(1+\alpha/R)^2]U(\epsilon,\vec{p})=\delta(\vec{p})-z^{-2}\sum_{\vec{\delta}}\sum_{\vec{\delta}'}U(\vec{p}+\vec{\delta}+\vec{\delta}')\ . \tag{54}$$

Both Eqs. (53) and (54) are useful to check the results. With the definition $x=[(1+\alpha/R)^2-\epsilon^2]^{1/2}$, the expressions for U in and below the spin-wave band are

$$U(\epsilon,\vec{p})=-iF(x,\vec{p})/x\quad(0\leq\epsilon\leq 1+\alpha/R)\ , \tag{55}$$

$$U(\epsilon,\vec{p})=iF^*(x,\vec{p})/x\quad(-1-\alpha/R\leq\epsilon\leq 0)\ , \tag{56}$$

with

$$F(x,\vec{p})=\int_0^\infty e^{-ixs}Q(s,\vec{p})\,ds\ , \tag{57}$$

$$Q(s,\vec{p})=(2\pi)^{-2}\int_{-\pi}^{+\pi}d\phi_1\int_{-\pi}^{+\pi}d\phi_2e^{i\vec{p}\cdot\vec{\phi}}\cos(s\gamma_{\vec{k}}) \tag{58}$$

For energies above the spin-wave band we similarly have, with $y=[\epsilon^2-(1+\alpha/R)^2]^{1/2}$,

$$U(\epsilon,\vec{p})=\frac{1}{y}H(y,\vec{p})\quad(|\epsilon|\geq 1+\alpha/R)\ , \tag{59}$$

$$H(y,\vec{p})=\int_0^\infty e^{-ys}Q(s,\vec{p})\,ds\ . \tag{60}$$

Our task now is to calculate $Q(s,\vec{p})$ by expanding $\cos(s\gamma_{\vec{k}})$ and integrating over ϕ_1 and ϕ_2. With l and m defined by $\vec{p}=(l,m)$ in units of $a\sqrt{2}$, we find

$$Q(s,\vec{p})=i^{|l+m|+|l-m|}J_{|l+m|}(\tfrac{1}{2}s)J_{|l-m|}(\tfrac{1}{2}s)\ , \tag{61}$$

Here, the J's denote Bessel functions of integer order. This result is considerably simpler than the corresponding result for a 3-D system, which involves an infinite summation over products of four Bessel functions. Substantially outside the spin-wave band ($y > 2$), the function $U(\epsilon, \vec{p})$ can be evaluated directly without use of $Q(s, \vec{p})$ by expanding the integrand in Eq. (51) in powers of $1/y^2$, yielding

$$U(\epsilon, \vec{p}) = \frac{\delta(\vec{p})}{y^2} + \sum_n \frac{(-1)^n}{y^{2n+2}} \frac{1}{2^{4n}} \frac{(2n!)^2}{(n+l)!(n-l)!(n+m)!(n-m)!} , \tag{62}$$

with the lower limit of the summation set at max (l,m), or unity if $l = m = 0$. Equation (62) may serve as a check on the calculation using $Q(s, \vec{p})$.

The Green's functions of the pure system, or rather the functions $F(x, \vec{p})$ and $H(y, \vec{p})$, have been calculated for $\vec{p} = (0,0)$, $(1,0)$, $(1,1)$, $(2,0)$, $(2,1)$, and $(2,2)$, from which all Green's functions occurring in the Γ^0 matrix of dimension 13×13 have been determined. As $Q(s, \vec{p})$ is a real function, the real and imaginary parts of F may easily be separated [cf. Eq. (57)]. The integrands of both ReF and ImF are products of oscillating functions, which are slowly damping out with s, as may be observed from the asymptotic expansion of $Q(s, \vec{p})$,

$$Q^A(s, \vec{p}) = \frac{2}{\pi s}(-1)^{|l+m|}[1 + (-1)^{|l-m|} \sin s] . \tag{63}$$

Since numerically $Q^A(s, \vec{p})$ is more convenient to integrate than $Q(s, \vec{p})$, the integrals have been divided into two parts. Below s_0, chosen at a zero point of $Q(s, \vec{p})$, the exact Eq. (61) was used, while in the remainder above s_0 Eq. (63) was substituted. For the accuracy required (10^{-4}) the use of the asymptotic expansion was allowed for $s_0 > 1000$. In the interval 0 to s_0, first all zeros of the integrand were determined, and the integral was subsequently calculated by summation over the contributions between subsequent zeros. The asymptotic part of the integration can be written as

$$(\text{Re } F)_{\text{asymp}} = \frac{2}{\pi}(-1)^{|l+m|} \int_{s_0}^{\infty} \frac{\cos xs}{s} ds + \frac{1}{\pi} \int_{s_0}^{\infty} \frac{\sin[(1-x)s]}{s} ds + \frac{1}{\pi} \int_{s_0}^{\infty} \frac{\sin[(1+x)s]}{s} ds , \tag{64}$$

with a similar expression for the imaginary part. This may be converted to a fastly converging summation over an in turn fastly converging Euler series made up from the contributions between subsequent zeros of the respective integrands in Eq. (64). In this way an accuracy of 10^{-5} is readily attained. We finally note that for x close to unity $Q(s, \vec{p})$ becomes such a slowly oscillating function that s_0 had to be taken at least 3000.

In the computer evaluation, the higher-order Bessel functions are determined recurrently from J_0 and J_1. For small arguments this method is the more inaccurate the higher the order. Near $s = 0$ the use of the recurrent relation was therefore carefully restricted to its region of validity within certain limits. Equation (54), employed to test the numerical accuracy of the final results, appeared to hold within at least 10^{-4}. The function $F(x, \vec{p})$ is calculated at intervals in x of 0.025, decreasing to 10^{-4} for $x \approx 0$ and $x \approx 1$. The real part of $F(x, \vec{p})$ is presented in Fig. 10 for the $\vec{p}$ relevant to our 13-site cluster. It is noteworthy that at $x = 1$ $F(x, \vec{p})$ drops stepwise from unity to zero, which is due to the property

$$\lim_{x \uparrow 1} \text{Re } F(x, \vec{p}) - \lim_{x \downarrow 1} \text{Re } F(x, \vec{p}) = 1 \tag{65}$$

and the fact that Re$F(x, \vec{p})$, which is related to the imaginary part of $U(\epsilon, \vec{p})$ and thereby to the density of states, vanishes beyond $x = 1$. Equation (65) provides an important check on our computations. Similarly, the imaginary part of $F(x, \vec{p})$ is presented in Fig. 11. Here, a point of note is the behavior for small x. In fact,

$$\lim_{x \to 0} \text{Im } F(x, \vec{p}) = -(-1)^{|l+m|} \tag{66}$$

produces yet another test on the numerical process.

As to the functions $H(y, \vec{p})$, their evaluation is

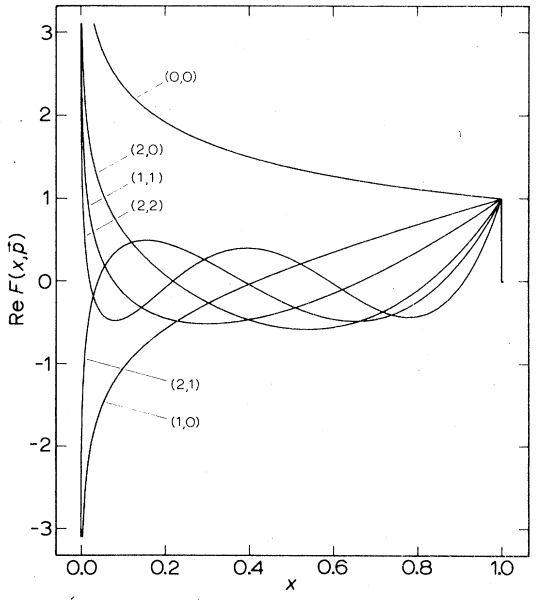

FIG. 10. Real part of the function $F(x, \vec{p})$ for various $\vec{p}$ in the three-shell cluster versus $x = [(1 + \alpha/R)^2 - \epsilon^2]^{1/2}$ with ϵ within or below the spin-wave band.

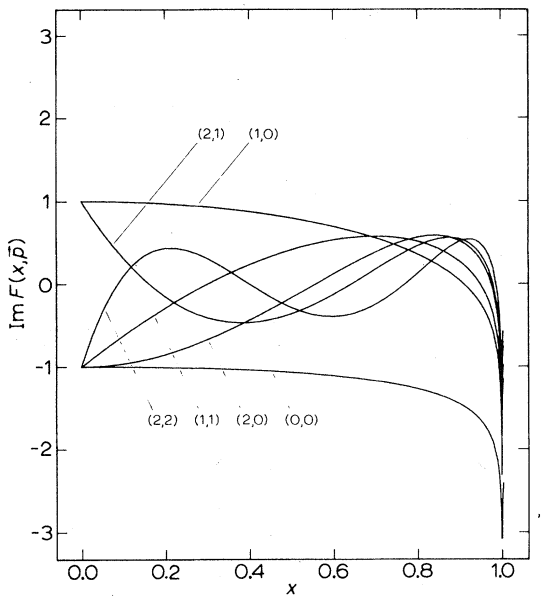

FIG. 11. Same as Fig. 10, but the imaginary part.

very similar to $F(x, \vec{p})$ except that the integral Eq. (60) converges fastly due to occurrence of e^{-ys}. They were calculated in the region $y \approx 0$ to 25, at intervals increasing from 0.002 to unity. The results are given in Fig. 12. For large values of y, $H(y, \vec{p})$ is almost entirely determined by the value of $Q(s, \vec{p})$ near $s = 0$. By use of the fact that at $s = 0$ all Bessel functions go to zero, except J_0, which becomes 1, we may for large y approximate $Q(s, \vec{p})$ by $\delta(\vec{p})$ to find $H(y, \vec{p}) \approx \delta(\vec{p})/y$. This approximative result may also be recovered from the first term of the direct expansion of $U(\epsilon, \vec{p})$ for large y in Eq. (62).

From $F(x, \vec{p})$ and $H(y, \vec{p})$, the Green's functions $U(x, \vec{p})$ for the pure system are finally obtained by use of Eqs. (55), (56), and (59), while $V(x, \vec{p})$ is derived from the various $U(x, \vec{p} + \vec{\delta})$ with Eq. (52). In turn, for the pure system, the imaginary parts of the Green's functions $\Gamma^0_{00}(\epsilon)$ for an up-sublattice site and $\Gamma^0_{11}(\epsilon)$ for an adjacent down-sublattice site equal $U(x, \vec{p})$ with $\vec{p} = (0, 0)$ multiplied by $\epsilon + 1 + \alpha/R$ and $\epsilon - 1 - \alpha/R$, respectively. They are displayed in Fig. 13. The equivalence of the up and down sublat-

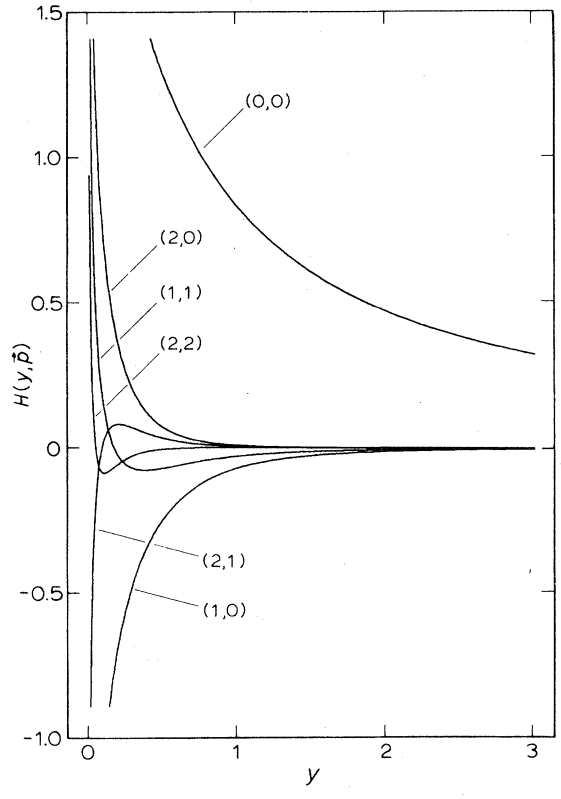

FIG. 12. Function $H(y, \vec{p})$ for various $\vec{p}$ vs $y = [\epsilon^2 - (1 + \alpha/R)^2]^{1/2}$, with ϵ above the spin-wave band.

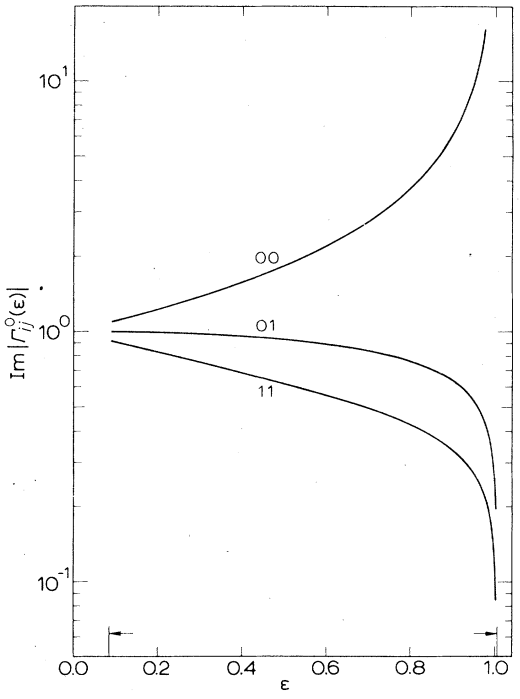

FIG. 13. Imaginary parts of Green's functions of the pure quadratic lattice Γ^0_{ij} vs the energy. Labels denote ij. The spin-wave band, $(2\alpha/R + \alpha^2/R^2)^{1/2} \leq \epsilon \leq 1 + \alpha/R$, is indicated by arrows; $\alpha/R = 0.0037$ at $T = 0$ appropriate to K_2MnF_4. Γ^0_{00} refers to a spin-up site, Γ^0_{11} to a spin-down site; Γ^0_{01} expresses the correlation between up and down sites. As to the signs, $\mathrm{Im}\Gamma^0_{ii}(\epsilon) < 0$ and $\mathrm{Im}\Gamma^0_{01}(\epsilon) > 0$ for $\epsilon > 0$. The part of the figure for negative ϵ has been omitted; $\mathrm{Im}\Gamma^0_{00}(-\epsilon) = -\mathrm{Im}\Gamma^0_{11}(\epsilon)$, $\mathrm{Im}\Gamma^0_{11}(-\epsilon) = -\mathrm{Im}\Gamma^0_{00}(\epsilon)$, $\mathrm{Im}\Gamma^0_{01}(-\epsilon) = -\mathrm{Im}\Gamma^0_{01}(\epsilon)$.

tices in the pure system is expressed by $\mathrm{Im}\Gamma^0_{00}(\epsilon) = -\mathrm{Im}\Gamma^0_{11}(-\epsilon)$. Also displayed in Fig. 13 is the imaginary part of the pure-system's Green's function $\Gamma^0_{01}(\epsilon)$, which involves the correlations between nearest neighbors and is directly found from $V(x, \vec{p})$ with $\vec{p} = (\frac{1}{2}, \frac{1}{2})$. The imaginary parts of $\Gamma^0_{01}(\epsilon)$ for positive and negative energies are identical except for the signs. Consequently, the integral of $\mathrm{Im}\Gamma^0_{01}(\epsilon)$ over the energy vanishes, as it should according to the sum rule Eq. (30) since the commutator between the local spin deviation operators a_0 and b_1 is zero.

To conclude the evaluation of the pure-system's Green's functions, it is of interest to note a striking difference between the present result for $\mathrm{Im}\Gamma^0_{00}(\epsilon)$ in the 2-D square lattice and that in a typical 3-D system, such as bcc.[2] In two dimensions at the bottom of the band, i.e., $\epsilon = \pm(2\alpha/R + \alpha^2/R^2)^{1/2}$, $\mathrm{Im}|\Gamma^0_{00}(\epsilon)|$ is close to unity, or more precisely, $\epsilon + 1 + \alpha/R$. In 3-D systems, by contrast, calculations reveal that $\mathrm{Im}|\Gamma^0_{00}(\epsilon)|$ sharply decreases to zero when approaching the band bottom. The physical interpretation is clearly found in the density of states $D(\epsilon)d\epsilon$, of which $\mathrm{Im}\Gamma^0_{00}(\epsilon)$ essentially is a representation. In three dimensions, $D(\epsilon)d\epsilon$ goes to zero proportional to k for small k, whereas in two dimensions $D(\epsilon)d\epsilon$ is a constant near the zone center.

B. Impurity-associated Green's functions

The magnetizations in the first three shells about the impurity are recovered from the local density of states, as represented by the imaginary parts of the corresponding Green's functions [cf. Eq. (45)], by carrying out the integral over the energy in Eq. (46). For the pure systems, of course, contributions to the integral only arise from energies within the spin-wave band, i.e.,

$$(2\alpha/R + \alpha^2/R^2)^{1/2} < |\epsilon| < 1 + \alpha/R \quad .$$

Apart from changes of the Green's functions within the band, the impurity may give additional contributions to the integral from poles in the Green's functions, i.e., zeros in $D(\epsilon)$, or rather its real part, occurring in the denominator when inverting the matrix $I - \Gamma^0 V$. These poles may lie within (nonmagnetic impurities) as well as outside the spin-wave band, the latter case corresponding to local modes (for Ni impurities above the band). They are of s, p, or d character, depending on the part of $D(\epsilon)$ having a zero. Note that outside the spin-wave band $D(\epsilon)$ is real.

To determine the number of states of a pole at $\epsilon = \epsilon_p$ outside the band, $[\Gamma(\epsilon)]^{-1}$ is expanded to first order about ϵ_p to find

$$\Gamma(\epsilon) = \lim_{s \to 0^+} \left[\frac{d\Gamma(\epsilon)^{-1}}{d\epsilon} \right]^{-1} \Big/ (\epsilon - \epsilon_p + is) \quad . \tag{67}$$

Integrating over ϵ, the pole contribution to the imaginary part of the Green's function may be expressed in the first derivative of its inverse,

$$-i\pi\delta(\epsilon - \epsilon_p) \left[\frac{d\Gamma(\epsilon)^{-1}}{d\epsilon} \right]^{-1} \quad ,$$

which is easily evaluated numerically. Within the spin-wave band, the imaginary part of $D(\epsilon)$ is generally of such a magnitude that substantial damping of the pole occurs. In this case, the contribution to the density of states is of course already included in the evaluation of the Green's function within the band. In the calculations, completeness of the density of states with inclusion of contributions from the poles has been tested by use of the sum rule Eq. (30), or rather its equivalent for the Γ's,

$$-\pi^{-1} \int \mathrm{Im}\Gamma_{AB}(\epsilon) d\epsilon = g_j \langle [A, B] \rangle \quad , \tag{68}$$

with j referring to operator B, yielding zero for Γ_{01}, and unity for Γ_{00}, Γ_{11}, Γ_{55}, and Γ_{99}. The sum rule indeed proved to be an important test on pitfalls in the considerable computational task. Any departure of more than 10^{-4} was taken to indicate trouble. In particular, the sum rule is a sensitive test on the local modes. The zeros of $D(\epsilon)$ as well as $d\Gamma(\epsilon)^{-1}/d\epsilon$ have been determined to an accuracy of 10^{-4} with an eight-point interpolation of the Green's functions near ϵ_p. For the required accuracy, the energies at which the functions $H(y, \vec{p})$ have been evaluated (Sec. IV A), generally were sufficiently dense. At some points, however, a new calculation of the $H(y, \vec{p})$ with more refined energy intervals about the pole was necessary to ascertain sufficient accuracy of the results.

The computation of the magnetizations has been done in an iterative way.[27] First, the parameters Δ, μ, and R of the pure system were determined iteratively. Subsequently, for the impure system the positions of the poles were iterated simultaneously with the expectation values $\langle a_0^\dagger a_0 \rangle$, $\langle b_1^\dagger b_1 \rangle$, and $\langle a_0 b_1 \rangle$, occurring in the perturbation parameters τ, σ, and λ. Both iteration processes were performed in three cycles, although in the third cycle the parameters did not change beyond the required accuracy of 10^{-4}. Finally, we have calculated the s, p, and d pole contributions to the density of states, if any, and obtained $\langle a_0^\dagger a_0 \rangle$, $\langle b_1 b_1^\dagger \rangle$, $\langle a_5^\dagger a_5 \rangle$, and $\langle a_9^\dagger a_9 \rangle$ by integrating over the imaginary part of the Green's functions Γ_{00}, Γ_{11}, Γ_{55}, and Γ_{99}, respectively, by use of Eq. (46).

Absolute values of the imaginary part of the Green's functions for our 2-D system containing a nonmagnetic impurity in the origin, are presented in Fig. 14 for the first three shells about the impurity. The Green's functions Γ_{01} and Γ_{00} are not presented, because they are zero in the absence of magnetic in-

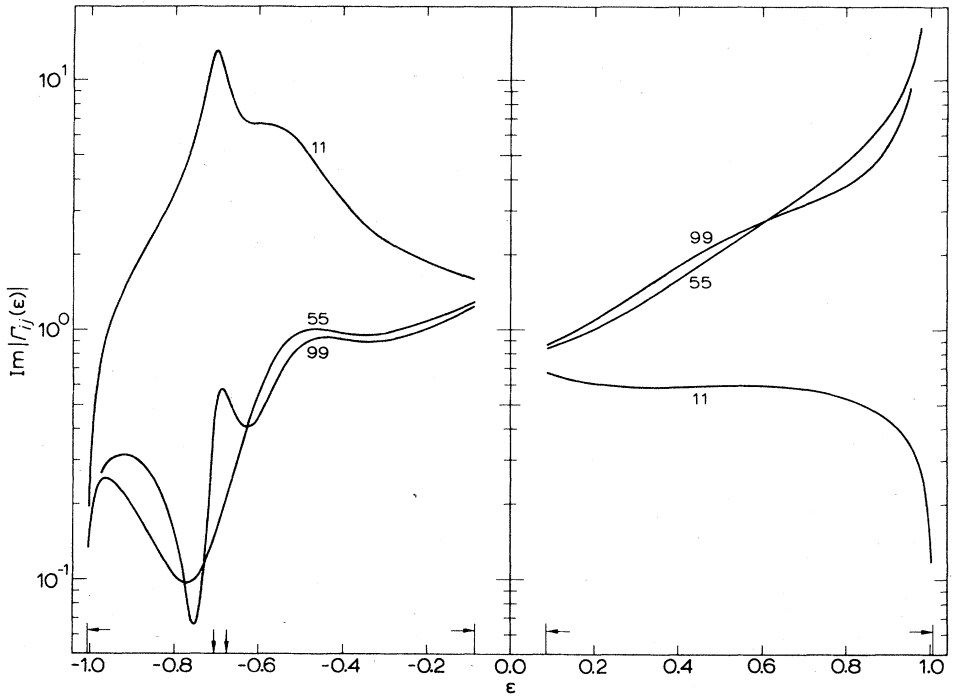

FIG. 14. Imaginary parts of the Green's functions for the first three shells about a nonmagnetic impurity in a quadratic lattice versus the energy. Signs are as in Fig. 13. Note the strong effects of the poles at $\epsilon=-0.675$ and -0.705 (vertical arrows), associated with p and d symmetry, respectively. By the absence of magnetic interactions involving the impurity, Γ_{00} and Γ_{01} are zero.

teractions of the impurity. For negative energies, the Green's functions are strongly shaped by poles, lying at $\epsilon=-0.675$, and -0.705, and originating from the p and d parts of $D(\epsilon)$. Because these poles lie within the spin-wave band, the associated extrema are generally shifted and broadened by the imaginary part of $D(\epsilon)$. Γ_{11}, describing the magnetization at the first neighbor of the impurity, still shows clearly distinguishable resonances with minor shifts only. A rough estimate of the pole positions may be obtained from molecular-field-type considerations. In this concept, the energy is that required for a single flip of a spin in the exchange field of its nearest neighbors. For a pure system we thus find an energy of $4|J|S$, but for a nearest neighbor of a nonmagnetic impurity we have $3|J|S$, the number of magnetic neighbors being reduced to three, i.e., $\epsilon=-0.75$ for the pole position, close to the result of the Green's-function calculation. Note that the energy is negative because the spin flip occurs at the nearest neighbor of the impurity, which lies on a down sublattice site. As to the temperature dependence of the magnetization $\langle S_1^z \rangle$, we anticipate from inspection of Fig. 14 relative to Fig. 13 a more rapid fall than in the pure system due to the increased density of states at low energies. For the further shells of neighbors the effects are clearly less pronounced. We return to this quantitatively in Sec. V B.

For the case of a Ni impurity, we present the Green's functions Γ_{00}, Γ_{01}, Γ_{11}, Γ_{55}, and Γ_{99} in Fig. 15, adopting $J_0/J=3.0$ for the Ni-Mn exchange interaction as will be discussed in Sec. V B, and using $\alpha_0=0.011$ $(T=0)$ for the anisotropy at the Ni site, resulting from AFMR experiments in K_2NiF_4,[28] but corrected for the change in dipolar anisotropy. Admittedly, in this choice lattice deformations are ignored, but the value is believed to be nearly correct. Moreover, the anisotropy appears to have only minor effects on the results. The poles of the Green's functions are now located above the spin-wave band. The local s mode, residing mainly on the impurity itself, occurs at $\epsilon=2.87$. Again the molecular-field approach, which predicts $\epsilon=J_0/J=3.0$, is in fair agreement with Green's functions. Comparing the density of states at the Ni impurity with that in the pure system (cf. Fig. 13), we note the strong effects of the pole at $\epsilon=2.87$. In fact, 87% of $\int|\mathrm{Im}\,\Gamma_{00}(\epsilon)|\,d\epsilon$ is transferred to this local s mode, which by virtue of its high energy will hardly be populated. Consequently, the Ni magnetization will drop only slowly with tem-

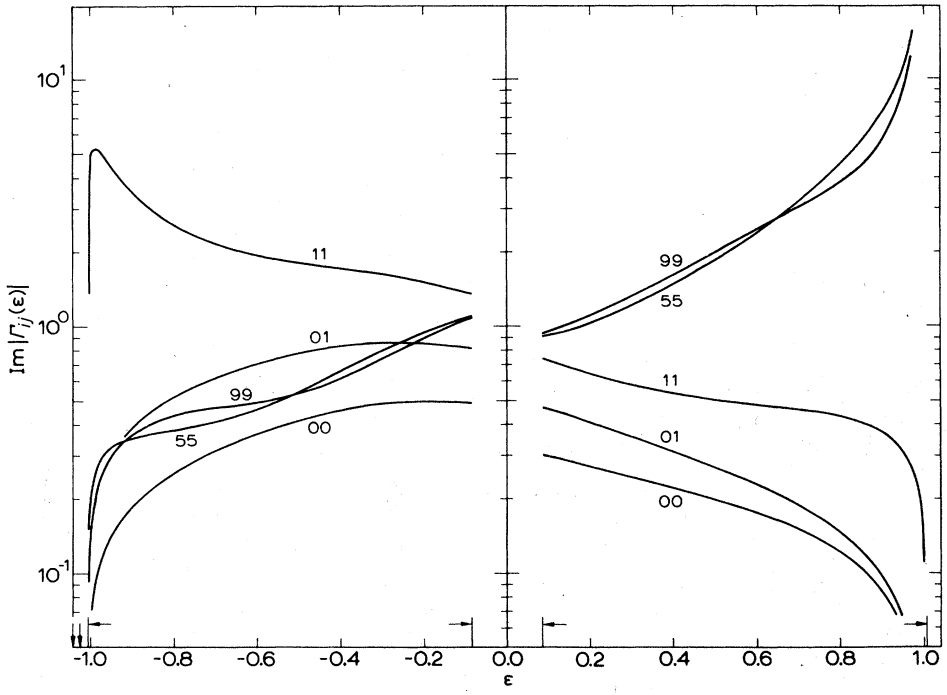

FIG. 15. Same as Fig. 14, but for a Ni impurity with $J_0/J=3.0$ for the impurity-host exchange interaction and zero-temperature values of the parameters $\alpha_0=0.011$, $\langle a_0^{\dagger}a_0\rangle=0.106$, $\langle b_1^{\dagger}b_1\rangle=0.160$ and $\langle a_0 b_1\rangle=-0.197$. Important contributions to $\mathrm{Im}|\Gamma_{00}|$ and $\mathrm{Im}|\Gamma_{01}|$ (87% and 31%, respectively) arise from a local s mode far above the spin-wave band at $\epsilon=2.87$ (cf. Fig. 13). Similarly, $\mathrm{Im}|\Gamma_{11}|$ indicates that a large fraction (38%) of the states at the first shell resides in local modes of p and d symmetry, lying just above the band at $\epsilon=-1.020$ and -1.037, (vertical arrows), respectively, at the expense of the density of states just below the upper band limit. The second and third shells are disturbed much more weakly.

perature, even when approaching the transition ($T_N\sim 42$ K). Quantitative results are again deferred to Sec. V B. Qualitatively, the slow decrease is of course also expected from the strong J_0 in the simple molecular-field picture. Additionally, p and d poles exist for $\epsilon=-1.020$ and -1.037, respectively, residing mainly on the first shell. Here, molecular field gives

$$\epsilon=-(3JS+J_0S_0)/4JS=-1.07\ ,$$

not distinguishing between p and d. As to the second and third shells about the impurity, $\mathrm{Im}\Gamma_{55}(\epsilon)$ and $\mathrm{Im}\Gamma_{99}(\epsilon)$ are quite similar to $\mathrm{Im}\Gamma^0_{00}(\epsilon)$ of the pure system. Also, the combined contributions of the local modes are of the order of 0.1% relative to contributions from within the spin-wave band. Consequently, the departure of the temperature dependences of $\langle S_5\rangle$ and $\langle S_9\rangle$ from $\langle S_\infty\rangle$ of the host are much smaller than for $\langle S_1\rangle$. For quantitative results, see Sec. V B.

V. COMPARISON THEORY-EXPERIMENT

A. Identification of the resonances

The identification of the various satellites of the main resonance is an essential part of our analysis, requiring careful judgment of various considerations, such as the intensities, the positions at zero temperature, and the dependences on temperature relative to the main resonance. The identification is complicated by the large number of satellites and their finite line width, limiting the resolution (cf. satellites 1 and 9 in Fig. 2). In particular, resonances close to the main resonance were hard to observe. Nevertheless, the resonances of the ^{19}F labeled in Fig. 1 could mostly be identified unambiguously.

First, let us consider the resonances originating from ^{19}F nuclei, adjacent to Mn sites in neighboring layers, i.e., the $^{19}F^{I}$ marked a' and a'' in Fig. 1, and the $^{19}F^{II}$ marked aa and ab. Because of the 2-D character of the K_2MnF_4 structure, these nuclei experience mainly dipolar fields from the impurity, which

are accurately known (Table I). Consequently, these resonances are generally very close to the calculated dipolar positions at both sides of the main resonance, as the Mn spin at site *a* may be parallel or antiparallel to the impurity. Other effects, such as lattice deformations and spurious hyperfine paths contribute only minutely, and weakly disturb the symmetry about the main resonance. The in-layer resonances *aa* and *ab* are seen in Figs. 4–6, the out-of-layer *a'* and *a''* in Figs. 7–9. Additional confirmation is found in the temperature dependence of these shifts relative to the host, which closely follows the sublattice magnetization of the pure system.

As we already discussed in Sec. II B, the ^{19}F nuclei adjoining Mn sites in the same layer as the impurity are subject to substantial shifts by lattice deformations, which are not known *a priori*. The resonance positions at zero temperature are therefore not a reliable starting point for identification. However, the ^{19}F adjoining the Mn at site 1, i.e., $^{19}F^{I}_{(1)}$, $^{19}F^{II}_{(15)}$, and $^{19}F^{II}_{(19)}$, may straightforwardly be identified from the temperature dependence of the shift because the magnetization at $Mn_{(1)}$ varies more strongly than that of the host. Using this criterion, the assignment to $^{19}F^{I}_{(1)}$ in Figs. 7–9 is indeed easily made. In Sec. V B the identification is further supported by comparison with the Green's-function calculations. As to the in-layer $^{19}F^{II}$ (Figs. 4–6), two strongly temperature-dependent resonances are observed, clearly associated with $^{19}F^{II}_{(15)}$ and $^{19}F^{II}_{(19)}$, both adjoining the first Mn neighbor. As site 15 occurs twice as often as site 19, identification is further done on the basis of intensity. From inspection of Figs. 7–9, it is seen that the temperature dependences of the resonance shifts of $^{19}F^{I}$ in further shells are very similar. Identification is therefore made upon the grounds of intensity and the assumption that the effects of lattice deformations fall off with the distance from the impurity. As $^{19}F^{I}_{(5)}$ and $^{19}F^{I}_{(9)}$ have equal occurrence, the latter assumption is, by necessity, the criterion for their assignment. We finally note, that identification of the ^{19}F directly associated with the impurity, i.e., $^{19}F^{I}_{(0)}$ and $^{19}F^{II}_{(01)}$, is quite simple as they are well isolated from the main resonance and its satellites.

B. Green's-function results

1. Nonmagnetic impurities

In Figs. 16 and 17 we present the experimental and calculated $\Delta S_1(T)$, $\Delta S_5(T)$, and $\Delta S_9(T)$, representative for the temperature-dependent parts of the local spin shifts in the first three shells of Mn ions about a nonmagnetic impurity. It is observed from the figures that, relative to the pure system, all three Green's-function approaches predict a more rapid decrease with temperature of the local sublattice magnetizations. Obviously, any reasonable treatment, in-

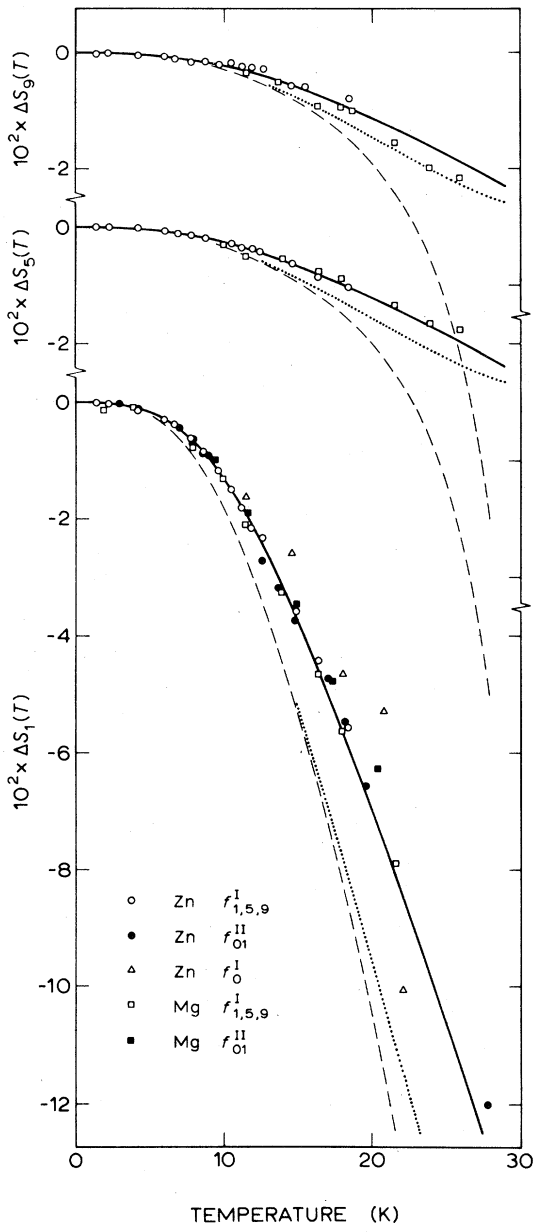

FIG. 16. Temperature-dependent part of local spin shifts, $\Delta S_i(T)$ [cf. Eq. (2)], in the first three shells about the nonmagnetic impurities Zn (0.4 and 0.8at.%) and Mg (2.2at.%). Experimental points are extracted from the weak satellites in the out-of-layer $^{19}F^{I}$ spectra, reworked according to Sec. II B. Additional data on $\Delta S_1(T)$ are from the $^{19}F^{II}_{(01)}$ and $^{19}F^{I}_{(0)}$ resonances, the latter only for Zn and with a large error (3×10^{-2}). Solid curves represent results of Green's function calculations on a 13-site cluster including nearest-neighbor correlations. Results of calculations with the correlations explicitly set to zero ($\mu = \langle a_0 b_1 \rangle = 0$) as well as those with a 2-D adaptation of Walker *et al.* (Ref.2) are indicated as dashed and dotted curves, respectively.

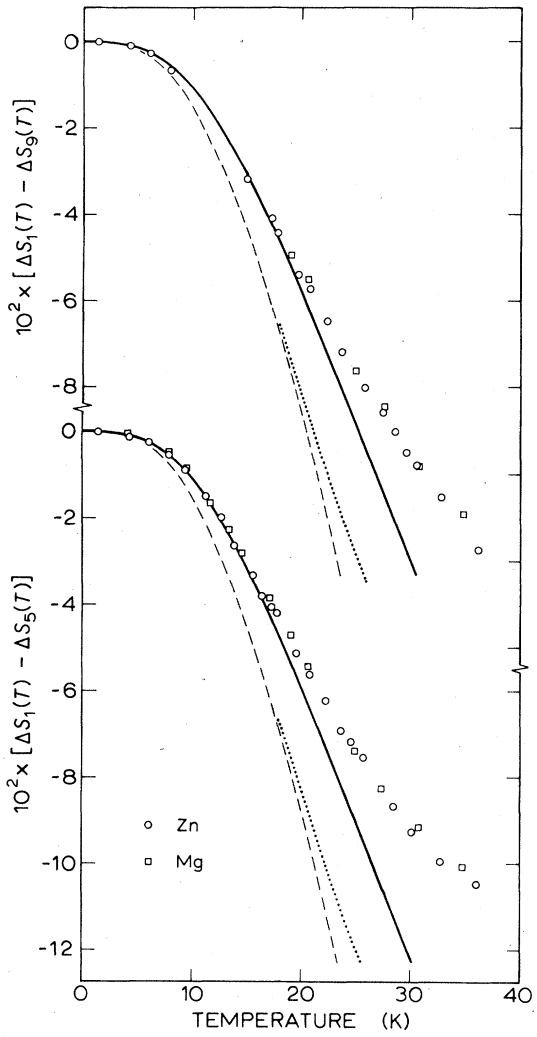

FIG. 17. Same as Fig. 16, but for $\Delta S_1(T) - \Delta S_i(T)$ ($i = 5, 9$), as recovered from the in-layer $^{19}F^{II}_{(1i)}$ satellites.

cluding the molecular-field approach, is expected to follow such a behavior. It is of more interest therefore to compare experiment and theory quantitatively.

On the experimental side, the spin shift at the first shell, $\Delta S_1(T)$, has independently been determined from the NMR at two different ^{19}F positions, *viz.*, $^{19}F^{I}_{(1)}$ and $^{19}F^{II}_{(01)}$. Additional information on $\Delta S_1(T)$ is entered in Fig. 16 from the $^{19}F^{I}_{(0)}$ resonance in the Zn-doped crystals, but with substantially reduced accuracy because of the smallness of second-neighbor hyperfine interaction (see Sec. II B). Experimental data on $\Delta S_5(T)$ and $\Delta S_9(T)$ are extracted from the corresponding $^{19}F^{I}$ resonances only. In Fig. 17 we present their behavior relative to $\Delta S_1(T)$ as taken from the 15 and 19 $^{19}F^{II}$ resonances. A particular point of note is that the experimental data in the 0.4- and 0.8-at.% Zn-doped crystals and those in the 2.2-at.% Mg-doped specimen are coincident with each other despite the differences in concentrations and lattice deformations. This further supports the correctness of the heuristic procedure of Sec. II, designed to eliminate the effects of the impurity-induced changes in the primary and second-neighbor hyperfine interactions.

When comparing the Green's-function results with the data, it emerges that the present formalism gives excellent results up to say 20 K, or $\frac{1}{2}T_N$, at a point where $\Delta S_1(T)$ has dropped by 0.07 spin units. Recall that $\Delta S_1(T)$ is *additive* to the pure system, in which the magnetization has fallen by 0.21 units at this temperature, i.e., the magnetization on the first shell has dropped faster by $\sim \frac{1}{3}$. It is also at about this temperature that spin-wave theory of 2-D systems is known to fail because of the onset of fluctuations associated with critical behavior. It is further seen, in particular from their departure from the $\Delta S_1(T)$ data, that the other approaches, which neglect the correlations μ and $\langle a_0 b_1 \rangle$, overestimate the fall of the ΔS_i's. They deviate from the experimental findings beyond say 8 K, corresponding to a drop of $\Delta S_1(T)$ by $\sim$ 0.01 spin units. Properly accounting for the correlation apparently extends the upper limit of the fit by a factor of 2 in temperature, or even more dramatically by a factor of 6 when expressed in spin units. We also note in this context that with inclusion of the correlations the initial drop of the local magnetizations should indeed be slower, since the more refined the decoupling the higher the excitation energies. The small differences between the calculations with $\mu = \langle a_0 b_1 \rangle = 0$ and those following Walker *et al.* are primarily due to the quasiboson technique used by the latter authors, to which we return below.

2. *Ni impurity*

The experimental data, analogous to Figs. 16 and 17, are presented in Figs. 18 and 19. As to the calculations, they are somewhat more complicated than for nonmagnetic impurities because of the occurrence of magnetization at the Ni impurity itself. No precise information is available on the anisotropy at the impurity site α_0 and the exchange interaction between the impurity and the Mn in the first shell J_0. As already remarked, α_0 has only minor effects on the results. The simplistic relation $|J_0| = (J_{Ni}J)^{1/2}$, which is often used for an estimate of J_0, yields $J_0/J = 3.48$ with $J_{Ni} = -102.1 \pm 0.8$ K for pure K_2NiF_4.[7] The exchange interaction $J_0 \vec{S}_0 \cdot \vec{S}_1$ between the Ni impurity ($S = 1$) and its first Mn neighbor ($S = \frac{5}{2}$) thus is not much different from the Mn-Mn exchange in contrast to nonmagnetic impurities, for which $J_0 = 0$. As is reflected in the measured $\Delta S_1(T)$ (cf. Figs. 16 and 18), the perturbation of the system is in fact smaller

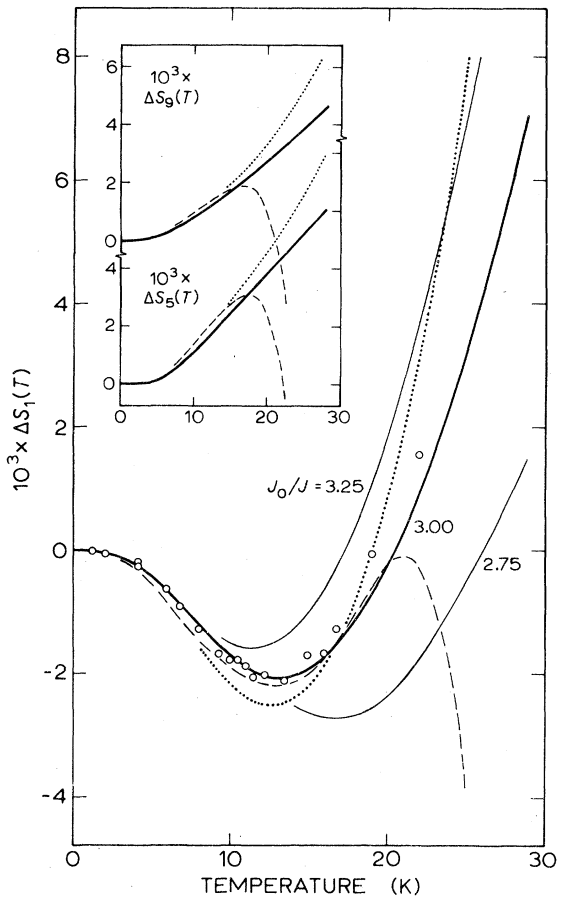

FIG. 18. Temperature-dependent part of local spin shifts in 0.5-at.% Ni-doped K_2MnF_4. Data points are derived from f_1^{I}. Note that $\langle \delta S_1(0) \rangle = 0.011$ [cf. Eq. (1)] exceeds $\Delta S_1(T)$, i.e., $\langle S_1(T) \rangle$ is larger than $\langle S_\infty \rangle$ at any T. Solid curves are Green's-function results on a 13-site cluster for $J_0/J = 3.00$, with $\alpha_0 = 0.011$ at $T = 0$. Thinner solid curves indicate the variation with the Mn-Ni exchange J_0. For dashed and dotted curves, see caption to Fig. 16. Resonances from further shells could not be identified; results of calculations are given in the inset.

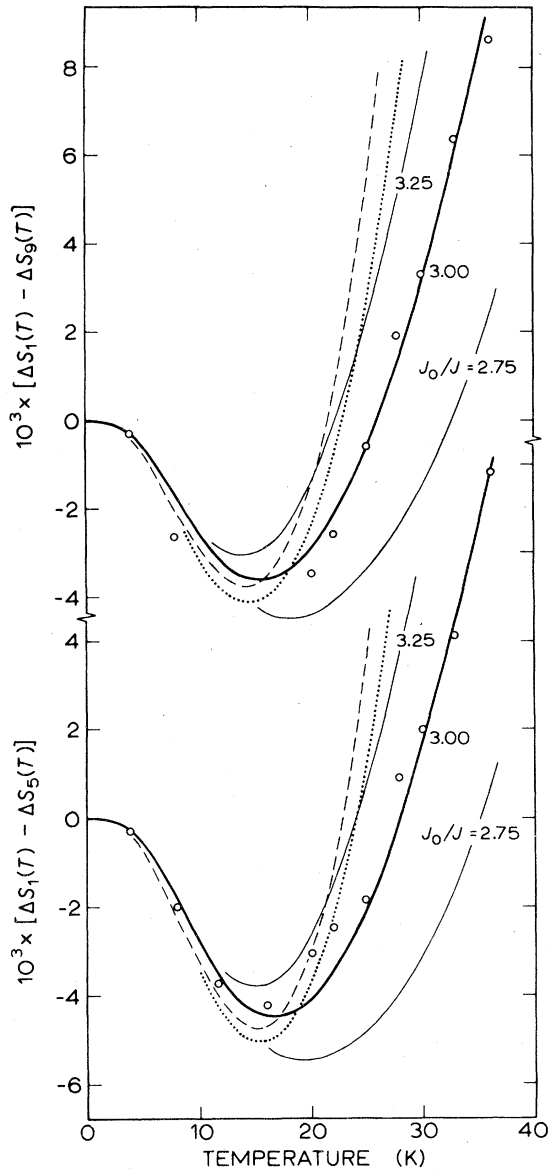

FIG. 19. Same as Fig. 18, but for $\Delta S_1(T) - \Delta S_i(T)$ ($i = 5, 9$), as recovered from the $^{19}F^{\mathrm{II}}_{(1i)}$ satellites. Concentration of Ni is 2.5at.%.

by about an order of magnitude relative to the nonmagnetic impurities. In the Green's-function calculations the Ni-Mn exchange J_0 is a parameter to be fitted to the experimental data. In Figs. 18 and 19 the effects of a variation in the exchange are indicated by plotting the results for $J_0/J = 2.75$, 3.00, and 3.25. With the experimental errors and other uncertainties taken into consideration, we arrive at $J_0/J = 3.0 \pm 0.1$. With this value, the $^{19}F^{\mathrm{I}}_{(1)}$ data (Fig. 18) are correctly described up to $\sim \frac{1}{2} T_N$, beyond which the resonance was lost. The $^{19}F^{\mathrm{II}}_{(15)}$ and $^{19}F^{\mathrm{II}}_{(19)}$ data (Fig. 19) are described successfully over the entire range of temperatures in which they were observed, i.e., up to 36 and 32 K, respectively. Note that the J_0 found is $\sim$15% lower than the geometric mean.

At the Ni site, we find from the calculations $\langle S_0^z \rangle = 0.894$ (Table III) at $T = 0$ K, or a local zero-point spin reduction of 0.106. This is considerably smaller than the spin-wave value of 0.171 for the square lattice, with the value of α appropriate for pure K_2MnF_4. (A simple second-order perturbation calculation with the Néel state as ground state yields 0.158; this is relegated to the Appendix). Taking the

hyperfine interaction between Ni and $^{19}F^{l}_{(0)}$ to be equal to that in pure K_2NiF_4, our results then predict the zero-temperature zero-field NMR to occur at 168.8 MHz, increased from 155.4 MHz in pure K_2NiF_4. With continuous NMR at 1.2 K the resonance was actually detected at 165.650 ± 0.020 MHz. The agreement is perhaps somewhat fortuitous in view of the uncertainties in direct- and second-neighbor hyperfine couplings by lattice deformations, but it anyway confirms the fact that the zero-point spin reduction is reduced at the Ni site.

The $^{19}F^{l}_{(0)}$ resonance, although very weak, could be tracked up to 19 K. This permits a very direct measurement of the temperature dependence of the magnetization residing at the impurity itself. The data points normalized to $T=0$ are given in Fig. 20, which also contains the corresponding Green's-function results. Note that there are no adjustable parameters, once J_0 is fixed. Yet, the result of the present Green's-function approach is again in excellent agreement with the data. It is further seen in Fig. 20 that, quite similarly to what we have found for the first few shells about the nonmagnetic impurities, the omission of nearest-neighbor correlations results in an overestimation of the fall of the magnetizations.

The temperature dependence of the Ni magnetization is intermediate between those in the pure systems K_2MnF_4 and K_2NiF_4. The slower drop with temperature of the Ni magnetization relative to the host is a direct consequence of the high density of states in the localized s mode, lying far above the spin-wave band ($\epsilon=2.87$, cf. Fig. 15). The density of states within the band has similarly been lowered, which in turn reduces the number of thermally excited magnons (it also diminishes the zero-point spin reduction, commented on above, to which essentially the *entire* zone contributes). In Raman spectra of 4.7-at.% Ni-doped K_2MnF_4 Lehmann *et al.*[29] found a line at 194.4 ± 1.0 cm^{-1}, which clearly is to be identified with the s mode. In our calculations, we found for the energy of the s mode 179 cm^{-1}, with an error of ~ 6 cm^{-1} propagated from the uncertainty in J_0. The origin of the disparity is not understood, but it is not unlikely that it has to do with the relatively high concentration used in their experiment, or the occurrence of clusters, for which Ni ions in K_2MnF_4 seem to have a certain preference.[30]

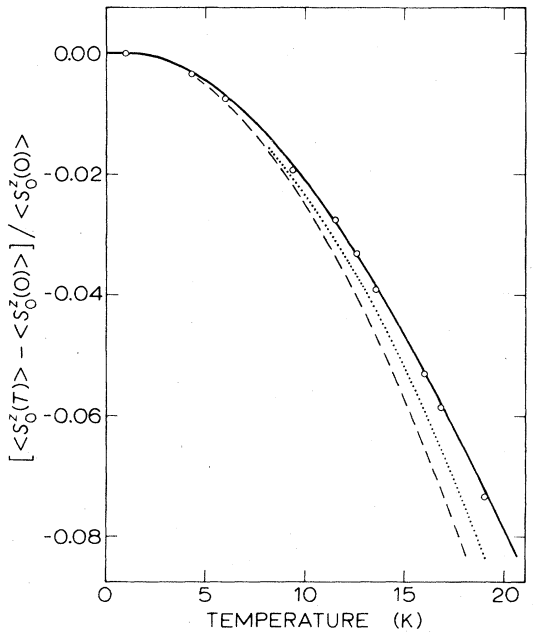

FIG. 20. Temperature-dependent part of the Ni magnetization in 0.5-at.% Ni-doped K_2MnF_4. Data points are derived from $^{19}F^{l}_{(0)}$ NMR, corrected to zero field. For curves, see caption to Fig. 16.

As to the magnetization at the first shell, the calculations show that at any temperature $\langle S^z_1(T)\rangle$ is *larger* than the magnetization of the pure system $\langle S^z_\infty(T)\rangle$. One might loosely say that by virtue of the Ni-Mn exchange the first shell is "dragged" by the Ni rather than the host. If we consider $\langle S^z_1(T)\rangle$ in detail (cf. Fig. 18 and Table III), we see that at 1 K the increment relative to the host amounts to 0.011 units of spin ($J_0/J=3.0$), decreasing to 0.009 units at 13 K. Returning to the Green's functions, we note that this corresponds to the increase, relative to the pure system, of $\mathrm{Im}|\Gamma_{11}|$ (Fig. 15) at low energies in the negative energy domain, which permits a larger number of long-wavelength excitations. Above 13 K, the region of higher energies becomes of importance, where $\mathrm{Im}|\Gamma_{11}|$ has been reduced substantially, partly by transfer of spectral density to the local modes. Then, the magnetization of the Ni^{2+} ion diverges rapidly from the host upon increasing the temperature, as is observed in the bending over of $\Delta S_1(T)$ towards higher values (Fig. 18). Calculations of $\Delta S_5(T)$ and $\Delta S_9(T)$ indicate these to increase without an initial drop.

The magnetizations at shells further out than the first could unfortunately not be measured. In the spectra (Fig. 9), some seven lines have been detected, all having positions that vary with temperature at least three times as strongly as calculated for the second shell. The origin of these resonances is not known as yet, but their stronger shifts with temperature suggest them to be due to Ni pairs. The only resonance that possibly, but not definitively, could be assigned to the second shell is the one lying at 65 G at $T\approx 0$ K, increasing to 100 G at 15 K.

A point of particular interest is that towards higher temperatures the formalism of Walker *et al.* starts to deviate from our formalism with $\mu=\langle a_0 b_1\rangle=0$. In fact, it more closely follows both the experiment and our calculations with μ and $\langle a_0 b_1\rangle$ included. In par-

TABLE III. Zero-temperature magnetizations in pure K_2MnF_4 and on the 13-site cluster in the impure K_2MnF_4, as calculated with Green's functions according to Sec. III with inclusion of nearest-neighbor correlations, the results of similar calculations but with the correlations explicitly set to zero ($\mu = \langle a_0 b_1 \rangle = 0$), as well as the results of a 2-D adaptation of the formalism of Walker *et al.*

Model	$\langle S^z \rangle_{\text{pure}}$	$\langle S_0^z \rangle$	$\langle S_1^z \rangle$	$\langle S_5^z \rangle$	$\langle S_9^z \rangle$
			Nonmagnetic impurity		
Present formalism	2.3292	· · ·	−2.3392	2.3121	2.3153
$\mu = \langle a_0 b_1 \rangle = 0$	2.3305	· · ·	−2.3404	2.3134	2.3166
Walker *et al.*	2.3303	· · ·	−2.3401	2.3133	2.3164
			Ni impurity ($J_0/J = 3.00$)		
Present formalism	2.3292	0.8940	−2.3402	2.3281	2.3296
$\mu = \langle a_0 b_1 \rangle = 0$	2.3305	0.8955	−2.3411	2.3291	2.3309
Walker *et al.*	2.3303	0.8970	−2.3405	2.3288	2.3303

ticular this has been observed for the Ni-doped system (Figs. 18–20), but as already remarked also applies to the nonmagnetic systems (Figs. 16 and 17). The deviations are clearly associated with the quasiboson technique utilized by Walker *et al.*, since their decoupling is equivalent with ours when $\mu = \langle a_0 b_1 \rangle = 0$. To verify this, we incorporate the quasiboson concept in our formalism in a retrospective way. By analogy with Walker *et al.*, we define a quasiboson of energy Y by $(e^{\beta Y} - 1)^{-1} = S - \langle S^z \rangle$, with $\langle S^z \rangle$ calculated in the approximation $\mu = \langle a_0 b_1 \rangle = 0$, and subsequently calculate a new value for the magnetization by use of the Brillouin function

$$\langle S^z \rangle = (S + \tfrac{1}{2}) \coth [(S + \tfrac{1}{2})\beta Y] - \tfrac{1}{2} \coth (\tfrac{1}{2}\beta Y) \quad . \tag{69}$$

The results of Eq. (69) are indeed coincident with those according to Walker *et al.*, except at high temperatures ($T > 30$ K) because we have not used the quasiboson mechanism iteratively. Apparently, in the formalism of Walker *et al.* the usage of quasibosons largely compensates the effects of the simpler decoupling scheme.

In Fig. 21 the resonance frequency of the $^{19}F^{II}$ intermediate between the Ni impurity and a first-neighbor Mn is displayed versus temperature. It reflects the magnetizations at both these sites with weights proportional to the respective hyperfine interaction constants. That is,

$$f_{01}^{II}(T) = |A_{Mn}^{II} \langle S_1^z(T) \rangle + A_{Ni}^{II} \langle S_0^z(T) \rangle| \quad , \tag{70}$$

where for convenience the nearest-neighbor dipolar interactions are included in the A's. From the corresponding pure systems, we have $A_{Mn}^{II} = 42.7$ and $A_{Ni}^{II} = 92.9$ MHz/(unit of spin), which combined with the Green's-function results for the magnetizations predicts $f_{01}^{II}(0) = 16.9$ MHz. Experiment, extrapolated to zero temperature, yielded 35.9 ± 0.1 MHz. The discrepancy clearly cannot be accounted for by uncertainties in the Green's-function results, but must be due to lattice deformations. Note that in the corresponding pure system the Ni-F^{II} and Mn-F^{II} distances

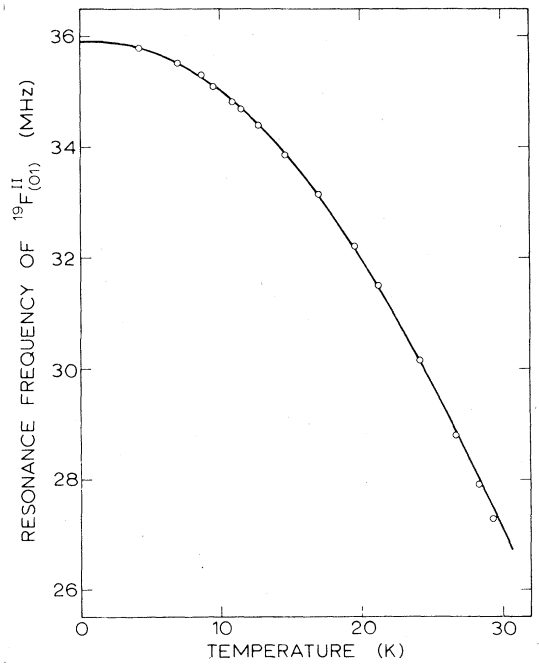

FIG. 21. Resonance frequency of $^{19}F^{II}_{(01)}$ intermediate between Ni and first-shell Mn in 2.5-at.% Ni-doped K_2MnF_4 vs temperature. Data are corrected to zero field. Solid curve represents the fit of Green's-function results with the hyperfine interactions as adjustable parameters.

are quite distinct, 2.003 and 2.086 Å, respectively, at $T=300$ K. In fact some information on the deformations may be extracted from $f_{01}^{II}(T)$. Using the calculated temperature dependences, $\langle S_0^z(T)\rangle$ and $\langle S_1^z(T)\rangle$, we may fit the A's to our data. The A's so obtained are $A_{Mn}^{II}=40.5\pm1.0$ MHz and $A_{Ni}^{II}=65.9\pm2.5$ MHz (solid line in Fig. 21), but strongly correlated; their ratio is 1.63 ± 0.05. In the doped system the Ni-$F_{(01)}^{II}$ hyperfine interaction has apparently dropped by $\sim 30\%$, corresponding to a dilation of ~ 0.06 Å, while the increase of the $Mn_{(1)}$-$F_{(01)}^{II}$ distance amounts to ~ 0.01 Å.

C. Main resonance shift

In our analysis, the positions of the satellite resonances are referred to that of the main resonance originating from ^{19}F far away from the impurity. In first instance, the main resonance is expected to coincide with the ^{19}F NMR of the pure lattice. The perturbation by the impurity is of local character, and indeed our calculations have shown that the perturbation drops off rapidly, at least within the first three shells. Remarkably therefore, a significant shift has been found of the main resonance relative to the pure host, even at zero temperature (Fig. 22). Within the errors, the shift is linear with the impurity concentration for a 2.5-at.% Ni-doped sample amounting to 2.5×10^{-3} units of spin. Evidently, the shift is not primarily related to lattice deformations. These would have similar effects in Ni- and Mg-doped crystals (both Ni^{2+} and Mg^{2+} have smaller ionic radii than Mn^{2+}), at variance with the findings. Additionally, the effects of lattice deformations on hyperfine interactions would have given shifts scaled with the sublattice magnetization (cf. Sec. II B), which decreases with temperature. It is noteworthy, however, that the temperature dependences of the main-resonance shifts, including the sign, resemble those of the corresponding local magnetizations in the first few shells. This clearly points to a magnetic origin.

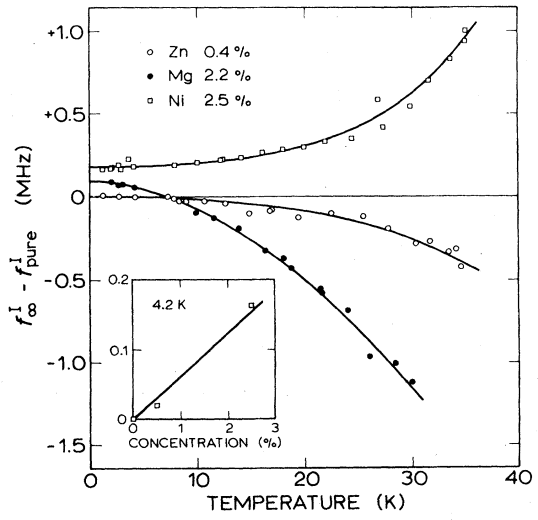

FIG. 22. Shift of the main resonance relative to the pure system vs temperature for 0.4-at.% Zn, 2.2-at.% Mg, and 2.5-at.% Ni-doped K_2MnF_4. The inset shows the variation of the shift vs the Ni concentration, indicating linear dependence. The shift vanishes for extreme dilution.

The perturbation of the pure host by the impurity, Eq. (19), has been taken to include the impurity–first-shell exchange and the alteration of the anisotropy at the impurity. It further includes the alterations of the local renormalizations up to the first shell, but explicitly does not include modifications in the exchange between further neighbors and renormalization at larger distances. The Green's-function apparatus is however such that it accounts for the fact that the magnetizations at further shells are affected as well, and in fact we have done the calculations for the first three shells. The shortcomings in the perturbation are therefore not believed to prevent alterations at substantial distance from being found. Note also that renormalization effects would disappear at $T=0$. Clearly, in order to calculate the main-resonance shift, more shells, say 10, should be included. Preferably, a distribution of impurities rather than a single one should be involved. This is however prohibitively difficult to treat.

For the sake of a qualitative analysis, it is of interest to consider which values of $\vec{k}$ contribute to the main-resonance shift. In this context, we note that in analogous 3-D systems, with MnF_2 as primary example, a shift of the host resonance has not been observed.[4] Apparently, the effect must ultimately bear on the 2-D character of the structure, i.e., be related to the finite density of states for long-wave components of the spin deviations. Let us therefore single out in the Brillouin zone a central domain of $\vec{k}$ corresponding to wavelengths larger than the mean impurity-impurity separation. The area occupied by this domain of course scales with the impurity concentration. For extreme dilution, it contracts to a very small fraction of the zone about $k=0$. In the remaining part of the zone, the perturbative action of the impurities may then be described by isolated single impurities, in the way treated in Sec. III, yielding spin deviations about the impurity of very localized nature superimposed on an unchanged host. In the central domain, however, the perturbation may be regarded as being uniformly spread over the lattice. Accordingly, the small-$\vec{k}$ part of the spin deviations will be uniformly shifted from the value in the pure system, with the shift linear in the impurity concentrations, and of course additive to the result originating from the large-$\vec{k}$ regime. Obviously, such a shift can only attain an observable magnitude in 2-D systems, where there is a finite density of states near the

TABLE IV. Exchange parameters and spin-wave energy gaps from fits of the host sublattice magnetization to renormalized spin-wave theory, and spin-wave gaps measured by AFMR extrapolated to zero temperature and field. The zero-temperature zero-field frequencies $f^1(0)$ are also given.

Impurity	$f^1(0)$ (MHz)	Spin-wave fit J'/k_B (K)	$\epsilon'_{k=0}(0)/k_B$ (K)	AFMR $\epsilon_{k=0}(0)/k_B$ (K)
Pure system	150.477 ± 0.003[a]	−8.41 ± 0.06[a]	7.54 ± 0.07[a]	7.40 ± 0.05[a]
0.4% Zn	150.472 ± 0.015	−8.30 ± 0.05	7.49 ± 0.08	7.27 ± 0.05
2.2% Mg	150.564 ± 0.017	−8.21 ± 0.05	7.32 ± 0.08	6.83 ± 0.05
2.5% Ni	150.638 ± 0.017	−8.39 ± 0.05	7.56 ± 0.08	7.31 ± 0.05

[a]Reference 7.

zone center. Earlier, the idea of uniformly distributing the perturbation, but in the *entire* zone, has been applied to random systems, such as $Mn_{1-x}Zn_xF_2$, in the so-called coherent-potential approximation.[5,31]

Experimentally, we indeed find for both the Ni-doped (0.5 and 2.5 at.%) and the Zn-doped (0.4 and 0.8 at.%) samples a shift of the main resonance which linearly increases with concentration. It should be stressed, however, that the local spin deviations, as expressed by the shift of the satellites relative to the main resonance in the spectrum, appeared to be *independent* of concentration. This conforms with the above model noting that the central small-$\vec{k}$ domain occupies only a small fraction of the Brillouin zone ($\sim 1\%$). In our analysis, we have therefore measured the position of the satellite resonances relative to the main resonance of the *impure* system itself rather than the resonance of the pure system.

The temperature dependence of the main-resonance frequency may be described in terms of a spin-wave formalism for the pure system, provided effective parameters are used for the exchange and the spin-wave energy gap at zero temperature, denoted by J' and $\epsilon'_{k=0}(0)$, respectively. This has been done following the earlier analysis of pure K_2MnF_4,[7] i.e., Oguchi renormalization and variation of the gap according to the sublattice magnetization have been included. This has resulted, as for pure K_2MnF_4, in excellent fits up to $\sim\frac{1}{2}T_N$, with the output values given in Table IV. Further, we have directly determined the gap from AFMR experiments, which essentially probe the $k=0$ mode. Results, extrapolated to zero temperature and field are entered in Table IV as $\epsilon_{k=0}(0)$. Upon inspection of $f^1_{(0)}$, J', $\epsilon'_{k=0}(0)$, and $\epsilon_{k=0}(0)$ for the nonmagnetic impurities, it appears that the variations relative to pure K_2MnF_4 are within the errors proportional to the concentration. The AFMR spin-wave gaps, of course more realistic than the ones from the spin-wave fit, are varying substantially. Referring to the analysis of the main-resonance shift above, we note that the strong effects of impurities on the AFMR are another indication of the special character of the central part of the Brillouin zone. The modification of the $k=0$ gap is not properly contained in the treatment of spin waves in Sec. III, but, as has been pointed out, is not likely to affect the calculated results as far as the *local* aspects are concerned.

D. Local susceptibilities

During the experiments some data have been collected on the field dependence of the resonance positions relative to the host (see, e.g., dashed and solid curves marked 1 in Figs. 7 and 9). These data essentially contain information on the susceptibility at the various shells about the impurity. They are somewhat fragmentary, and calculations have not been done. Yet, the data allow a number of interesting features to be discerned.

First, the impurity-induced modifications of the local susceptibilities appeared to be independent of the direction of the field, or equivalently, on whether the impurity is on the up or down sublattice. This is demonstrated in Fig. 23 for a 0.4-at.% Zn-doped system at 11.2 K, where the resonance positions, as before referred to the resonance of the ^{19}F far away from the impurity, are found to vary linearly with the external field, ranging from −10 to +10 kG. Note that a positive field is taken to correspond with the low-frequency Zeeman component, i.e., the down sublattice (having the Mn magnetic moment opposite to the field), and consequently a negative field with the up sublattice. Although the result seems to be quite obvious on the basis of molecular-field-type treatments, it is in fact not. A clear example of the

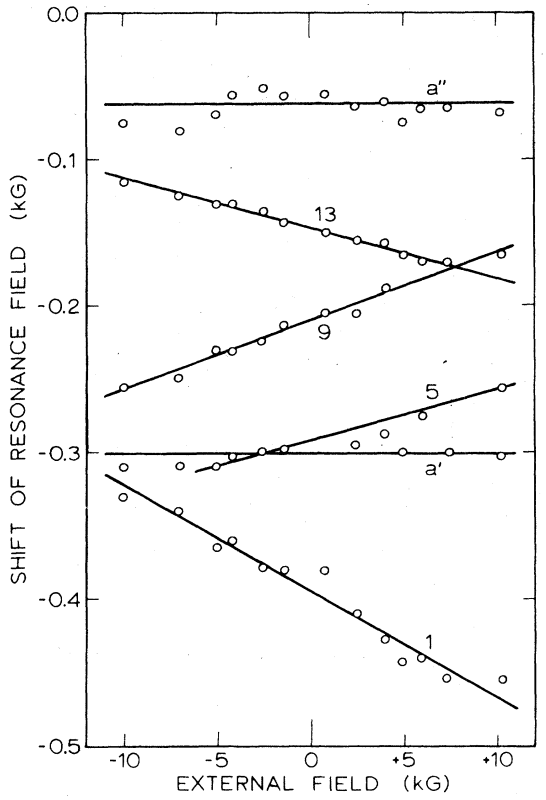

FIG. 23. Shift of resonance field, relative to the main resonance, of $^{19}F_{(i)}^{I}$ in the first four shells in 0.4-at.% Zn-doped K_2MnF_4 at 11.2 K vs external fie The slopes reflect the local susceptibility additive to the pure system. Note the invariance of the positions of dipolar lines.

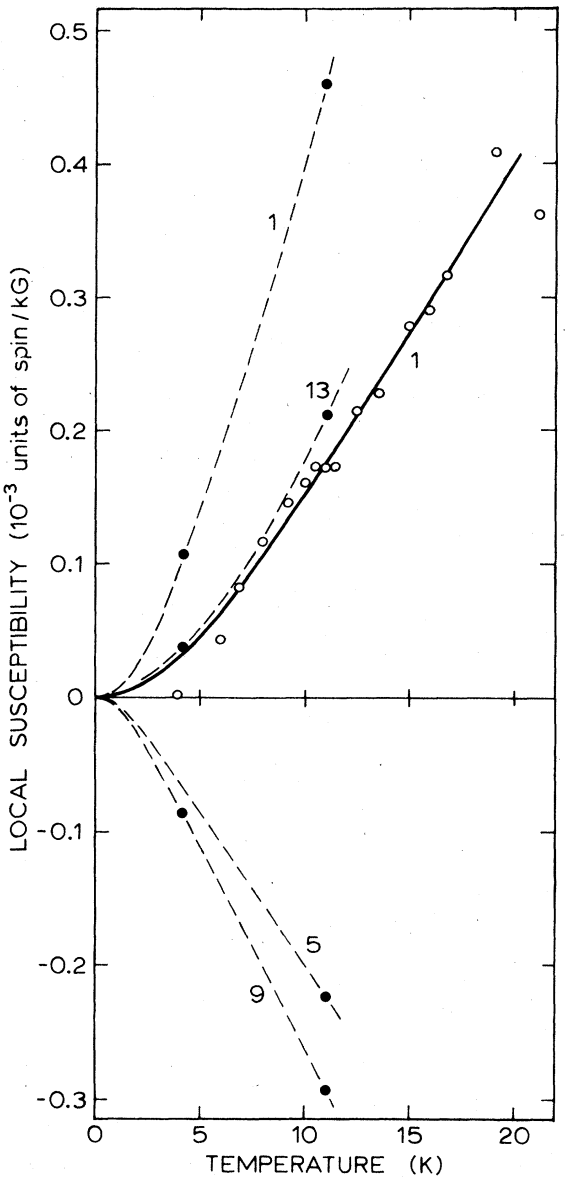

FIG. 24. Local impurity-induced susceptibility, additive to the susceptibility of the pure system, vs temperature in 0.4-at.% Zn-doped (closed circles) and 0.5-at.% Ni-doped (open circles) K_2MnF_4. Labels denote positions about the impurity.

contrary is supplied by the susceptibilities of the up and down sublattices of pure K_2MnF_4, which from ^{19}F NMR have been found to differ by about an order of magnitude below $\sim$ 15 K.[8] At 10 K and 10 kG, for example, the field-induced moments residing on the up and down sublattices of K_2MnF_4 are 0.4×10^{-3} and 2.7×10^{-3} units of spin, respectively.

The second point is also best documented with the results in the Zn-doped system. The impurity-induced susceptibility of the first four shells about Zn is given in Fig. 24, as derived from the slopes in Fig. 23 and a similar plot at 4.2 K. The figure also contains results for Ni. Note that the susceptibility of the pure system has to be added to the results in Fig. 24 to obtain the total local susceptibility near the impurity. With regard to the impurity-induced part of the susceptibility, the quite remarkable finding is that it is *negative* at the second and third shells. In other terms, given a field along the first-shell magnetization, on the introduction of an impurity the moments on the first few shells all grow in absolute magnitude, irrespective of whether they point upward or downward (or all diminish in case the field is opposite to the first shell). The changes differ of course for the various shells, and the net moment points along the field. This is quite contrary to anything anticipated from molecular-field approaches, and clearly must be associated with the nature of the excitations.

To understand the failure of the molecular-field approaches, it is instructive to compare some of their results with experiment. In molecular field the local

susceptibility at low temperatures is proportional to $e^{Y_l}/(e^{Y_l}-1)^2$, with

$$Y_l = \sum_{m(l)} |J_{lm}| S_m / k_B T \ ,$$

the summation running over the nearest neighbors of l. For T going to zero, the impurity-induced susceptibility diverges, but for higher temperatures molecular field appears to give a reasonable description for the nearest neighbors of a nonmagnetic impurity in 3-D systems.[4] In two dimensions with $J=-8.41$ K for the pure system and $T=10$ K, the susceptibility of the first shell about a Ni impurity would be reduced by $\sim\frac{1}{3}$ relative to the pure system, whereas in fact it is twice as large. (The pure system's susceptibility averaged over up and down sublattices is 0.15×10^{-2} units of spin at 10 K, and 0.5×10^{-2} units at 20 K and 10 kG.) In the Zn-doped samples the same model predicts the susceptibility at the first shell to be increased by a factor of about 7, while further neighbors are virtually unaffected. Experiment gives that the increment of the local susceptibility relative to the pure system at the first four shells amounts to +2.5, −1.3, −1.7, and +1.1, respectively, expressed in terms of the pure system's averaged susceptibility. Evidently, the local impurity-induced susceptibility extends to quite a distance from the impurity, a fact which molecular-field-type approaches do not account for. It is obvious that an alternative and more sophisticated treatment based on molecular fields would not improve matters.

VI. CONCLUDING REMARKS

The most salient fact emerging from the present investigation is that also in 2-D systems such a strong perturbation as the replacement of a Mn^{2+} ion by a nonmagnetic impurity has effects of very localized nature, apart from a concentration-dependent overall shift. The dimensionality of the magnetic lattice, having a profound influence on the number of long-wave length excitations, is of course expected to play a role. When comparing our 2-D results with those in a 3-D bcc system,[2] we indeed see that at the first shell the effects are larger by about half an order of magnitude. However, there certainly is no prolific change when going from three to two dimensions.

A Green's-function treatment that includes nearest-neighbor correlation was found to provide an excellent description of the variation with temperature up to $\sim\frac{1}{2}T_N$, as was seen from comparison with experimental data up to the third shell. Here, variation of the anisotropy according to AFMR results was taken into account. It should be emphasized that the modifications relative to the host system at shells further than the first are very small indeed. At the first shell about Zn, the thermal decrement of the magnetization, at say 20 K, amounts to 0.07 units of spin in addition to 0.21 already present in the unperturbed host; at the second and third shell the drop is ~0.01. For Ni, having an exchange with Mn only 15% higher than the primary exchange, the variation of the magnetization at the first shell relative to the host does not surpass 0.002 units of spin up to $\frac{1}{2}T_N$. The Ni impurity spin itself drops by ~0.07 at this point. In contrast to the temperature dependence, the local zero-point deviations could not be measured by NMR because they are indistinguishable from the effects of changes in the transferred hyperfine interactions associated with lattice deformations (measuring at the ^{55}Mn nucleus instead of the ^{19}F would not improve matters because the ^{55}Mn linewidth is quite large[32]). An exception to this is the zero-point reduction at the Ni impurity, which clearly is substantially smaller than that of the host. Considering the superb results of Green's functions for the temperature variation, however, there seems no reason to believe that the corresponding results for the zero-point reduction would be incorrect. These indicate (cf. Table III) that for both Zn and Ni the reduction at the first shell is diminished by ~0.01 from the pure value of 0.17. Note that at the first shell about Zn the shifts with temperature are substantially larger. The Ni itself has a reduction of only 0.11 because the density of states is largely transferred to a local mode above the band.

Another important result arrived at in comparing calculations to the data, is the necessity to account for the correlation between nearest neighbors. Ignoring the correlation, we found that the fall of the local magnetizations with temperature is overestimated, in particular at the first shell about a nonmagnetic impurity. Our results without correlation are very nearly the same as those obtained by suitable adaptation of the Green's-function formalism by Walker *et al.*, except for higher temperatures where their use of the quasiboson mechanism apparently starts to compensate the neglect of the correlation. At this point, however, the deviations are already large.

An interesting aspect further is the effect of an impurity on the magnetization at substantial distance, which in first approximation is proportional to the concentration. As such a shift has not been observed in 3-D systems, it seems to be typical for two dimensions. It is not contained in the present treatment, which has been worked out up to the third shell only, and must be related to excitations of long wavelengths. Characteristic differences of two and three dimensions are also reflected in the imaginary parts of the Green's function of the pure system, which in the former case converge to unity and in the latter rapidly fall to zero, demonstrating the dependence of the density of states on the dimensionality of the system.

ACKNOWLEDGMENTS

Financial support by the Netherlands Foundation for Fundamental Research of Matter (FOM) and the Netherlands Organization for the Advancement of Pure Research (ZWO) is gratefully acknowledged. The authors thank H. F. R. Arciszewski, J. W. C. Frösch, M. T. C. M. Sijbrand-Verhaak, and W. Twigt for assistance in taking the data. They have further benefited from discussions with T. M. Nieuwenhuizen on decoupling procedures.

APPENDIX: ZERO-POINT SPIN DEVIATION BY PERTURBATION THEORY

A rough estimate of the local zero-point spin deviations may be obtained from a simple second-order perturbation calculation, in which the Néel state is taken as the ground state, and the transverse exchange as the perturbation. We then have for the ratio of the deviation at the impurity to that of the host

$$\frac{\Delta_0}{\Delta_\infty}=\frac{S_0}{S}\frac{(8S-1)^2}{[(3J/J_0+4)S+S_0-1]^2} \quad . \tag{A1}$$

For a Ni impurity in K_2MnF_4, with $J_0/J=3.0$, $S=\frac{5}{2}$, and $S_0=1$, we then find $\Delta_0/\Delta_\infty=0.924$, as compared to 0.612 from the Green's-function calculations. In a similar second-order perturbation calculation, we obtain for the zero-point deviation at the first shell

$$\frac{\Delta_1}{\Delta_\infty}=\frac{3}{4}\frac{(8S-1)^2}{[7S+(J_0/J)S_0-1]^2}+\frac{\Delta_0}{4\Delta_\infty} \quad . \tag{A2}$$

For a Ni impurity this results in $\Delta_1/\Delta_\infty=0.943$, while the Green's function calculation yields 0.936. For a nonmagnetic impurity, we take in Eq. (A2) $J_0=0$, resulting in $\Delta_1/\Delta_\infty=0.994$ for $S=\frac{5}{2}$, to be compared with the Green's-function value of 0.942.

[1]T. Wolfram and J. Calaway, Phys. Rev. 130, 2207 (1963).
[2]L. R. Walker, B. C. Chambers, D. Hone, and H. Callen, Phys. Rev. B 5, 1144 (1972).
[3]S. Watarai and T. Kawasaki, J. Phys. Soc. Jpn. 32, 346 (1972).
[4]M. Butler, V. Jaccarino, N. Kaplan, and H. J. Guggenheim, Phys. Rev. B 1, 3058 (1970).
[5]R. A. Cowley and W. J. L. Buyers, Rev. Mod. Phys. 44, 406 (1972).
[6]R. J. Birgeneau, H. J. Guggenheim, and G. Shirane, Phys. Rev. B 1, 2211 (1970).
[7]H. W. de Wijn, L. R. Walker, and R. E. Walstedt, Phys. Rev. B 8, 285 (1973); erratum B 9, 2419 (1974).
[8]A. F. M. Arts, C. M. J. van Uijen, and H. W. de Wijn, Phys. Rev. B 15, 4360 (1977).
[9]With a Mn-F^I separation of 2.105 Å, summation of the dipolar fields over the up and down sublattices gives for the dipolar contributions to the $^{19}F^I$ hyperfine interactions, in the notation of Ref.8, $D_1=-16.13$ MHz and $D_1'=+0.19$ MHz (per unit of spin), respectively.
[10]B. O. Loopstra, B. van Laar, and D. J. Breed, Phys. Lett. 26A, 526 (1968); 27A, 188 (1968).
[11]A. J. van der Wal and H. W. de Wijn, Phys. Rev. B 20, 3712 (1979).
[12]G. B. Benedek and T. Kushida, Phys. Rev. 118, 46 (1960).
[13]C. Bucci, G. Guidi, C. Vignali, V. Fano, and M. Giordano, Solid State Commun. 10, 115 (1972).
[14]S. Ogawa, J. Phys. Soc. Jpn. 15, 1475 (1960).
[15]R. G. Shulman and K. Knox, Phys. Rev. 119, 94 (1960).
[16]T. P. P. Hall, W. Hayes, R. W. H. Stevenson, and J. Wilkens, J. Chem. Phys. 38, 1977 (1963).
[17]V. J. Folen, Phys. Rev. B 6, 1670 (1972).
[18]See, e.g., J. A. van Winsum, H. W. den Hartog, and T. Lee, Phys. Rev. B 18, 178 (1978).
[19]M. Arakawa, K. Horai, and Y. Shimizu, J. Phys. Soc. Jpn. 35, 1337 (1973); Nai Li Huang, R. Orbach, E. Simánek, J. Owen, and D. R. Taylor, Phys. Rev. 156, 383 (1967); W. Marshall and R. Stuart, Phys. Rev. 123, 2048 (1961).
[20]J. J. Davies, J. Phys. C 1, 849 (1968).
[21]R. K. Jeck and J. J. Krebs, Phys. Rev. B 5, 1677 (1972).
[22]The local susceptibilities in the vicinity of the impurity are indeed different from the host, as will be pointed out in more detail in Sec.V D. At this point, it is noteworthy that the impurity-induced modifications of the local susceptibility are invariant for inversion of the field, i.e., equal for spins on up and down sublattice sites. Consequently, the effect cancels by symmetrization.
[23]T. Oguchi, Phys. Rev. 111, 1063 (1958).
[24]S. W. Lovesey, J. Phys. C 1, 102 (1968).
[25]We note that in Ref.3 the sign of the energy is reversed with respect to this work and a different labeling of the sites is utilized. $G(a_2^\dagger a_2)$ and $G(b_1 b_1^\dagger)$ are the Green's functions of the impurity and its nearest neighbors, respectively, corresponding with the Green's function Γ_{00} and Γ_{11} in this work.
[26]L. R. Walker, B. B. Cetlin, and D. Hone, J. Phys. Chem. Solids 30, 923 (1969).
[27]In all calculations the anisotropies α and α_0 are taken to scale with the spin-wave energy gaps measured with AFMR. For AFMR in K_2MnF_4 see H. W. de Wijn, L. R. Walker, S. Geschwind, and H. J. Guggenheim, Phys. Rev. B 8, 299 (1973). The effects of α on the Green's functions are minor.
[28]R. J. Birgeneau, F. DeRosa, and H. J. Guggenheim, Solid State Commun. 8, 13 (1970).
[29]W. Lehmann and R. Weber, J. Phys. C 10, 97 (1977); W. Lehmann, thesis (unpublished).
[30]Besides the set of resonances in Fig. 9, there is evidence from Raman scattering [A. van der Pol and H. W. de Wijn (unpublished).]
[31]P. Soven, Phys. Rev. 156, 809 (1967); W. J. L. Buyers, D. E. Pepper, and R. J. Elliott, J. Phys. C 6, 1933 (1973); C. J. Coombs and R. A. Cowley, J. Phys. C 8, 1889 (1975).
[32]R. E. Walstedt, H. W. de Wijn, and H. J. Guggenheim, Phys. Rev. Lett. 25, 1119 (1970).